ADVANCED THEORY AND SIMULATIONS
www.advtheorysimul.com

Prey Impact Localization Enabled by Material and Structural Interaction in Spider Orb Webs

Vinícius F. Dal Poggetto, Federico Bosia, Gabriele Greco, and Nicola M. Pugno**

Spider webs are mechanical systems able to deliver an outstanding compromise between distinct requirements such as absorbing impacts and transmitting information about vibration sources. Both the frequency information and amplitude of input signals can be used by the spider to identify stimuli, aided by the mechanical filtering properties of orb webs. In this work, a numerical model based on nonlinear stress–strain constitutive relations for spider silk is introduced to investigate how the spider orb web allows spiders to detect and localize prey impacts. The obtained results indicate how the orb web center relative transverse displacements, produced by local resonance mechanisms, are used for precise localization, while nonlinear stress stiffening effects improve prey sensing. Finally, it is also shown that, although beneficial, a large number of radial threads may not be necessary for prey localization.

1. Introduction

Spiders are remarkable for the extraordinary use they make of silks and webs to obtain information about prey location, the presence of potential predators, and as channels to communicate with other spiders.[1,2] Distinct spider web geometries include the vertical orb web, funnel web, sheet web, and tangle web.[3,4] Spider orb webs are the product of evolutionary adaptation, and are able to deliver a compromise between different requirements, such as absorbing the impacts of prey while also efficiently transmitting information about the nature and position of vibration sources,[5] which the spider uses in addition to visual and olfactory information. Spider orb webs have proven to be one of the most inspiring systems to design novel structures able to manipulate elastic waves,[6–9] which further encourages the investigation of their complex mechanics.

Here, we consider a simple vertical orb web model constituted by radial threads, connecting the center of the web (hub) to the outer region (frame), and viscid threads (spiral) connecting adjacent radial threads.[10] These silk threads have distinct mechanical properties: radial (mainly composed of major ampullate silk) threads are known for high toughness and tensile strength, with higher Young's modulus and diameters, while spiral (flagelliform silk coated with aggregate glue, which makes them viscid) threads are known for their large ultimate strain, but have smaller Young's modulus and diameters.[11–13]

Radial threads are the most important vibration-transmitting elements, which also absorb most of the kinetic energy,[14] while spiral threads ensure that the prey remains in contact with the web, covering a wide catching area and coupling radial threads. Radial threads can undergo several types of motion, distinguished between i) transverse motion (perpendicular to the thread and the plane of the web) ii) lateral (perpendicular to the thread and in the plane of the web), and iii) longitudinal (along the thread axis).[5]

The frequency response in spider orb webs can present rather intricate characteristics, and some of them are summarized in[15–17]: i) longitudinal waves transmitted by radial threads have an attenuation of about 0.2 to 0.3 dB cm^{-1}, being 5 to 10 times smaller in wavelength than transverse and lateral waves; ii) oscillations caused by insect impacts contain most of the energy centered around 100 Hz; iii) peaks between 5 and 50 Hz are typical of struggling insects due to leg movement; iv) fluttering bees and flies produce peaks between 100 and 300 Hz; v) wind-induced vibrations are considerably lower in frequency (below 10 Hz); vi) both frequency and amplitude can be used to identify stimuli; vii) the gradient of signal amplitudes between the various threads can be used (20 to 30 dB), since viii) the differences in time of arrival at distinct threads may be too short (≈1 ms) to be noticeable. These characteristics suggest that spider orb webs have evolved to act as mechanical structures that present unique wave transmission and filtering abilities.[18]

V. F. Dal Poggetto, G. Greco, N. M. Pugno
Laboratory for Bioinspired, Bionic, Nano, Meta Materials & Mechanics,
Department of Civil, Environmental and Mechanical Engineering
University of Trento
Trento 38123, Italy
E-mail: v.fonsecadalpoggetto@unitn.it; nicola.pugno@unitn.it

F. Bosia
DISAT
Politecnico di Torino
Torino 10129, Italy

N. M. Pugno
School of Engineering and Materials Science
Queen Mary University of London
Mile End Road, London E1 4NS, UK

The ORCID identification number(s) for the author(s) of this article can be found under https://doi.org/10.1002/adts.202100282

DOI: 10.1002/adts.202100282

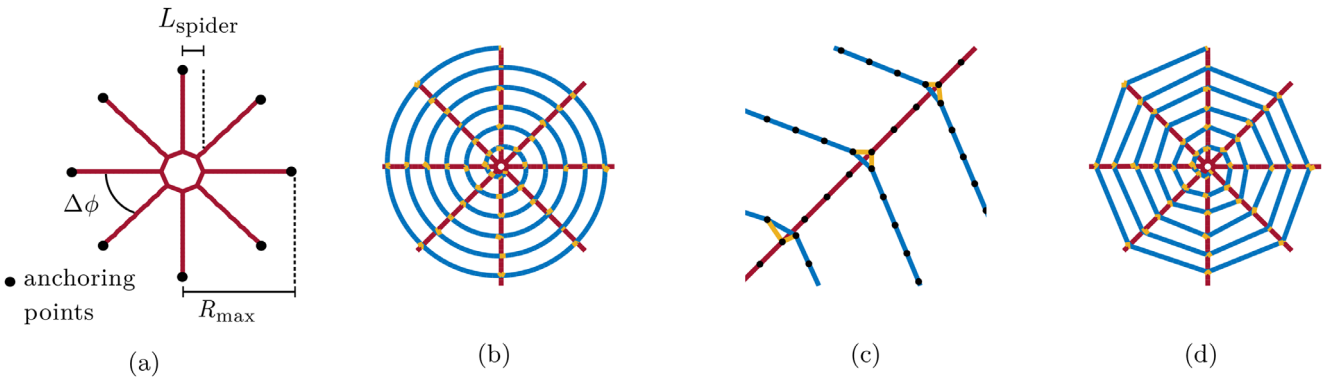

Figure 1. Process of assembly and stabilization of radial and spiral threads. The initial structure is assembled considering equally prestressed radial threads (■), connected to each other through their inner edges and restricted at their outer edges. a) The whole structure is circumscribed in a circle of radius R_{max}, with each of the n_ϕ radial threads apart from each other by an angle $\Delta\phi = 2\pi/n_\phi$. b) After applying a stabilization process to accommodate the pretensioned structure, n_s spiral threads (■) are disposed using an Archimedean spiral ($R(\phi) = \alpha\phi$) and gluing elements (■) are included. c) Gluing elements are used to connect spiral and radial threads when their distances are smaller than a given threshold. d) Due to initial stresses at spiral elements, an additional stabilization process is needed, leading to the stable final shape.

Another interesting feature that is indicative of spider adaptation is pre-stress, which can be adjusted to facilitate the sensing of smaller prey.[19] The study conducted by Mortimer et al.[20] using truss elements to reproduce the cable-like behavior of spider silk indicates that the prestress of radial threads can have significant effects on the sonic properties of webs. This can be partially explained by the fact that distinct waves speeds are governed by distinct mechanisms (transverse wave by string tension and mass density, and longitudinal waves by mass density and stiffness,[21] which is a physical behavior associated with wave propagation in strings, as we also demonstrate later). Also, Wirth and Barth[22] have demonstrated that radial thread prestress increases with the mass of the spider, considering both spiders of the same species and of different species, thus indicating this is a generally observed phenomena in spider orb webs. Although other phenomena such as supercontraction may play a major role in silk behavior,[23,24] we shall restrict our attention to radial and spiral threads with fixed stress–strain curves.

Kaewunruen et al. [25] proposed a numerical model to evaluate the natural frequencies and mode shapes of different spider orb web configurations. However, the same material properties were considered for both radial and spiral threads, and the spider mass was not accounted for in the analysis, which certainly has a major influence on the vibration response of the spider orb web.

In this work, we derive a simple model for an orb web to allow the investigation, using a wave propagation approach, on how prey-induced vibrations can be perceived at the orb web center. Considering energy conservation principles, this is implemented in a finite element (FE) method framework to perform both linear and nonlinear vibration analyses. In particular, it is possible to compute vibration modes and time-transient vibrations induced by prey impact.

2. Models and Methods

Without loss of generality, we will consider a common European spider species (*Araneus diadematus*) to obtain typical geometric and mass values to properly represent a spider web model. Even though this spider's orb web may present geometric asymmetry with respect to its center (hub),[26] we will consider here a structure with symmetric radial threads and almost symmetric (see below) spiral threads, so the implications of geometric asymmetry is not considered in the assessment of other effects. The model of the spider orb web is constructed using radial and spiral elements and the corresponding properties of dragline and viscid threads, respectively, with 1D elements connecting specific points (nodes). The web construction process is shown in **Figure 1**.

The geometric configuration of the spider orb web of radius R_{max} is initially modeled by n_ϕ pretensioned radial threads (red lines in Figure 1a), with angular distances $\Delta\phi = 2\pi/n_\phi$ and connected to each other at the orb web center (hub). Although symmetry has been shown to influence the spider's time of response, we consider it here as a simplifying hypothesis.[27]

To account for the position of the spider at the hub, nodes at this region are equidistant from the geometric center of the orb web, using a distance considered here as the representative size of a spider, given by L_{spider}. Due to the residual forces generated by prestressing, additional displacements may be required to produce the corresponding strain and stress configuration that yields equilibrium.

After stabilization, spiral threads are included in the model, connected to the radial threads using gluing elements (spiral threads in blue and gluing elements in yellow in Figure 1b). Gluing elements are considered to have the same characteristics of viscid silk, only serving to provide connections between radial and spiral threads, which is a simplifying hypothesis. Its actual behavior can be much more complex, as demonstrated by Greco et al.,[13,28] and may also be associated with prey retention.[29]

The superposed spiral has an angle-varying radius $R(\phi)$, obtained using an Archimedean spiral in the form

$$R(\phi) = \alpha\,\phi \tag{1}$$

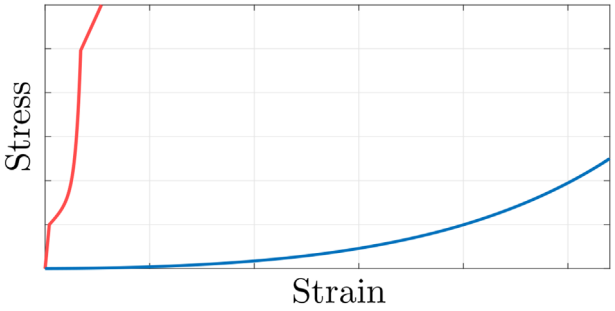

Figure 2. Stress–strain relations for (■) dragline and (■) viscid silk threads.

where α is a parameter defined according to the desired number of spirals n_s, given by

$$\alpha = \frac{R_{max}}{n_s\, 2\pi} \tag{2}$$

which yields $\phi \in [0,\ n_s 2\pi]$.

Gluing elements are created by checking, for each of the spiral nodes, which is the closest of the radial thread nodes, and if the distance between such nodes is smaller than a given tolerance, resulting in typically two connections per crossing between radial and spiral threads (Figure 1c). Once all elements are connected, the structure is once again stabilized with respect to internal forces now accounting for initial prestressing due to tensioned spiral threads, resulting in the typical final structure (Figure 1d).

Although some species use a specific signal thread and do not reside at the center of the orb web,[30] we will restrict ourselves to species exploiting wave transmission in the web. As already pointed out by Mortimer et al.,[31] the presence in the spider orb web of the spider mass itself greatly influences vibration transmission. For this reason, we also consider that, for a given spider mass m_{spider}, each of the innermost nodes of the radial threads is loaded with an additional mass equal to m_{spider}/n_ϕ. Even though the weight of a spider may greatly vary during its lifespan,[32] it is also true that larger spiders usually producer fibers with larger dimensions, which indicates a balance between these quantities.[33–35] Thus here a typical value is considered for the purpose of modeling.

Typical nonlinear stress–strain relations for the dragline and viscid threads are illustrated in **Figure 2**. Both stress–strain relations are numerically described in Supporting Information using the empirically parameterized data from.[10]

In the considered relations, the dragline silk stress–strain curve shows a relatively small linear region until yielding, followed by an exponential stiffening, and a region with affine behavior until failure. The stress–strain relation for the viscid silk thread displays a combination between linear and exponential behaviors.

Since the strain energy is dependent on the current stress state of considered threads, which increase due to displacements (displacement-induced strains and strain energy are derived in Supporting Information), this yields intrinsically nonlinear relations for the analysis of wave propagation in this type of structure. Thus, ideally, linear analyses considering constant-stiffness elements are only valid for very small input forces and may lose their validity as elements present increasing stresses.

To assess the effect of increasing stresses and their influence on wave propagation, two types of analyses are performed: i) linear and ii) nonlinear. In linear analyses i) stresses and strains are computed for an initial configuration and the transitory time analyses are performed considering no significant changes in element stresses. Nonlinear analyses ii) consider each material's stress–strain curve. Thus, the difference between fully linear and nonlinear analyses is that in the latter, the computed displacements induce additional stresses which have a stiffening effect on the structure (stress stiffening), while in the former, this effect is negligible.

The derivation of mass and stiffness matrices (accounting for both longitudinal stiffness and stress-induced stiffening effects) necessary to perform time-dependent analyses is presented in Supporting Information. The description of the iterative processes for the structure stabilization due to residual internal forces and for time-series computations is given in Supporting Information.

Since in this work we are only concerned with structure-bourne vibrations (as opposed to vibrations associated with fluid interactions[36–38]) and slit sensilla in spiders perform similar functions as that of strain gauges,[39] acting as high-pass filters to attenuate very low-frequency signals typical of environmental noise,[40] it seems only natural to consider the outputs of our simulation as those perceived in the central region of the structure. Due to the nonlinear nature in the constitutive relations of the threads forming the orb web, when considering nonlinear analyses, various input displacements must be tested to assess the variation in the web response.

3. Results and Discussion

3.1. Parameters

For the construction of the spider orb web, we have considered an outer radius of $R_{max} = 200$ mm, $n_\phi = 8$ radial divisions, and $n_s = 25$ spiral turns. Radial and spiral threads have radii of 3.93 μm and 2.40 μm, respectively,[10] while the mass density is the same for both, namely $\rho = 1300$ kg m^{-3}.[20] Although differences in the pre-stressing of radial threads may occur depending on their relation with the surrounding supporting structure, these differences can be considered negligible when compared to the overall stress values.[20] Thus, we consider equally prestressed radial threads with two distinct levels: i) 100 MPa and ii) 150 MPa, both representing states that occur before yielding. Spiral threads have a single prestress of 10 MPa. Boundary conditions are imposed as zero displacements at the outer edges of radial threads considering all directions. Regarding dimensions and mass of the spider, since typical sizes of the *Araneus diadematus* also vary greatly (ranging from 6.5 to 20 mm in females and 5.5 to 13 mm in males,[41]) we will consider a representative value, given by a typical length of $L_{spider} = 10$ mm, with a mass of $m_{spider} = 20$ mg,[31] which is considerably larger than the web mass (0.49 mg). **Figure 3** shows the spider orb web structures obtained after

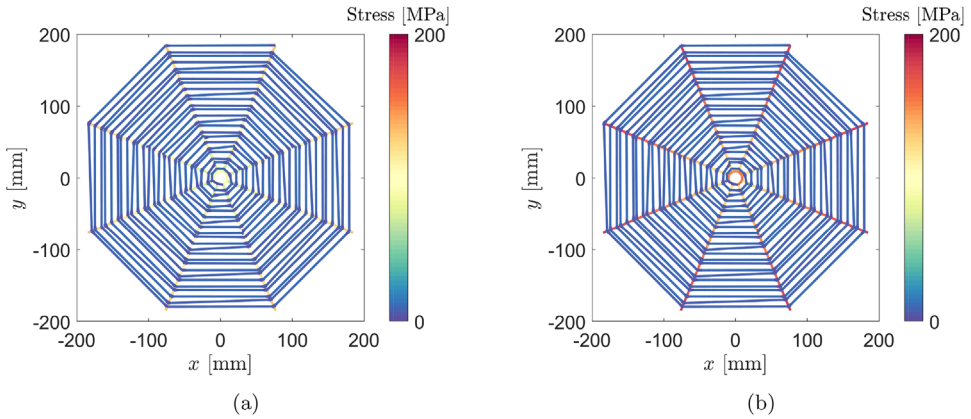

Figure 3. Stable structures (deformations due to initial stress are suited to yield equilibrium) for a) 100 and b) 150 MPa.

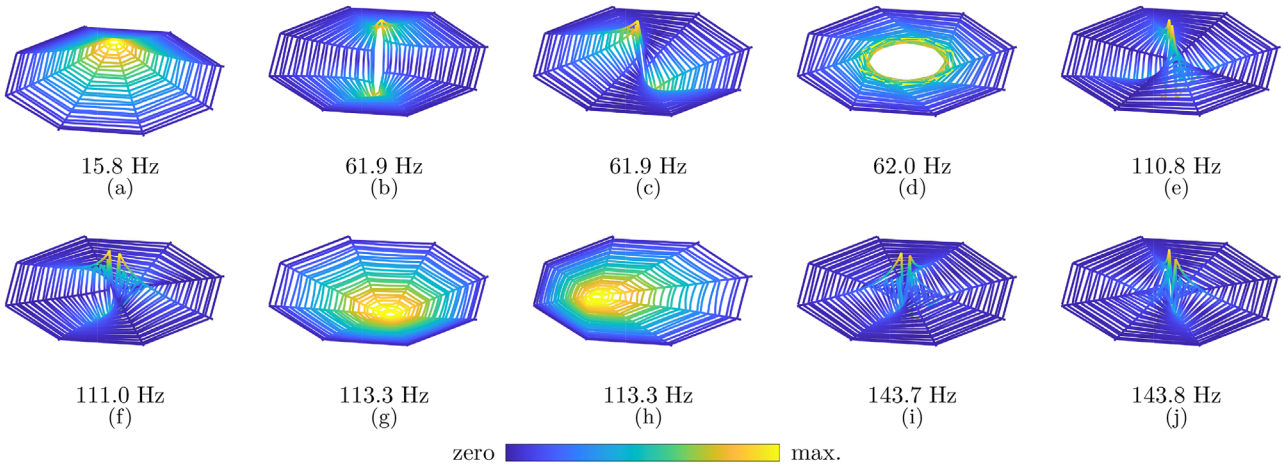

Figure 4. Modes of vibration and natural frequencies considering only the orb web and spider masses. Mode (a) is a transverse displacement mode; modes (b) and (c) represent bending modes; mode (d) is a torsional mode; modes (e), (f), (i), and (j) are second order-like bending modes, and modes (g) and (h) are in-plane translational modes. Colors indicate zero and maximum values of absolute displacements.

applying the stabilization procedures for balancing initial prestresses. Although some variation in the final prestress of radial threads can be observed, these differences are small.

3.2. Modal Analysis

Figure 4 presents the modes of vibration and natural frequencies of a spider web considering a 100 MPa prestressing on radial threads prior to any given impact, that is, considering only the structural properties and the spider mass equally distributed at central nodes.

These vibration modes can be interpreted as transverse (15.8 Hz), bending (61.9 Hz), torsional (62.0 Hz), second-order bending (110.8, 111.0, 143.7, and 143.8 Hz), and in-plane modes (113.3 Hz). The orb web is mainly responsible for the system stiffness associated with the observed modes and frequencies, since its inertia effects are negligible when compared to the spider mass. It is interesting to notice that when considering the first three modes, the highest frequency associated with out-of-plane displacements is 61.9 Hz, yielding a fundamental period of 16.2 ms, which indicates that input forces with a duration considerably smaller than this can be interpreted as short pulses.

The main influence of the increase in prestressing of radial threads (150 MPa) is a 23% increase in the natural frequency of the transverse displacement mode and a 29% increase for bending modes (both first and second order-like). In-plane modes also present an increase in their natural frequencies, but since we assume prey impact in the orthogonal direction to the orb web plane, they probably do not play a part in prey location and are not discussed here.

We now consider the presence of a prey such as a *Drosophila* fly (0.2 mg, of the same order of magnitude as described in the literature,[42] about 1% of the total mass of the spider) modeled as a point mass added in distinct positions at spiral threads. This mass is sufficiently small not to change significantly the previously observed modes of vibration and frequencies (smaller than 0.06% variation for the first three natural frequencies). However, the addition of this mass introduces additional modes

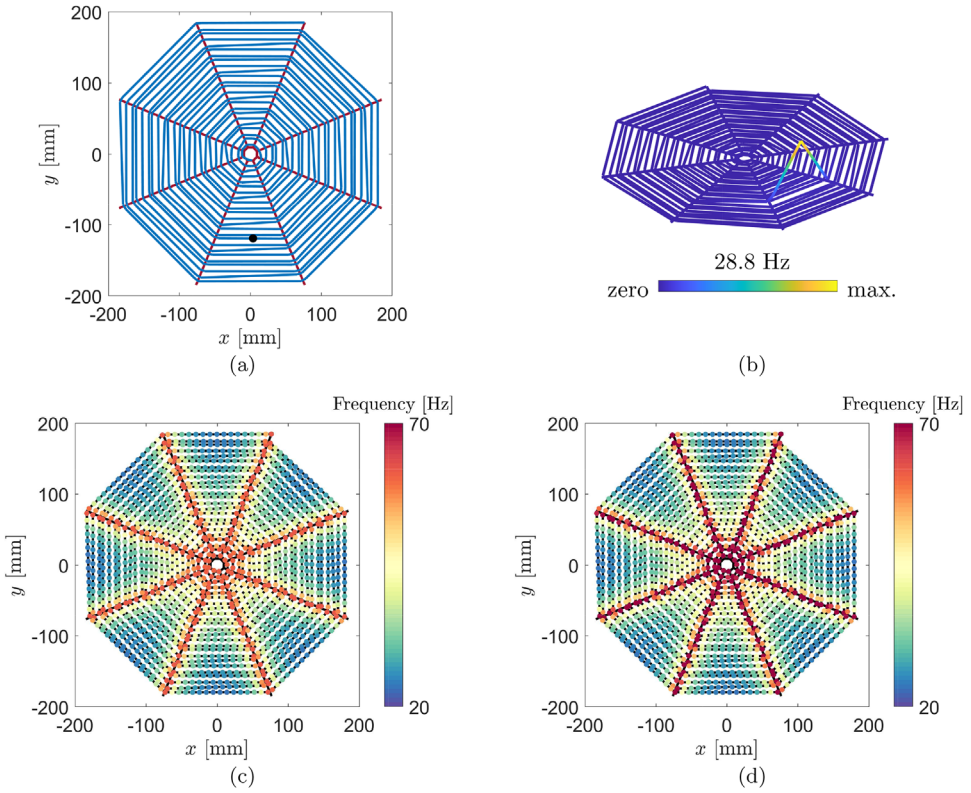

Figure 5. Locally resonant out-of-plane transverse mode and frequencies due to prey impact. a) An example of prey location with its b) corresponding locally resonant out-of-plane normal mode indicating a frequency of 28.8 Hz. Colors indicate zero and maximum values of absolute displacements. c) Colormap indicating impact points with corresponding resonant frequencies on the orb web domain for a radial thread pre-stress of 100 MPa. d) Same as (c), but with a prestress of 150 MPa.

corresponding to the displacement of the prey mass in the same (longitudinal) and in the orthogonal (transverse) direction as the spiral thread where it is located. **Figure 5** shows a possible prey location, the mode of vibration and natural frequency of the introduced out-of-plane transverse mode for 100 MPa prestressed radial threads. Following the same reasoning, we also construct a map corresponding to the resonant frequencies associated with the out-of-plane transverse mode due to the inclusion of prey mass at each impact point separately, for both 100 and 150 MPa pre-stressed radial threads.

Figure 5a shows an example of an impact position, that is, location for the addition of prey mass, which introduces an additional out-of-plane transverse displacement vibration mode with a natural frequency of 28.8 Hz, as shown in Figure 5b. The map of resonant frequencies (Figure 5c) which shows that i) the distribution of resonant frequencies is fairly regular considering each pair of adjacent radial threads, which is due to the web symmetry; ii) the resonant frequency is minimal at the center of each spiral thread and increases toward adjacent radial threads; iii) for a fixed angular direction, resonant frequencies increase for points closer to the orb web center, which is explained by the smaller length of the corresponding spiral thread.

When considering the influence of an increased value of prestress for radial threads (150 MPa, Figure 5d), the most notable effect is the increase of resonant frequencies at points in the vicinity of radial threads. This indicates that radial threads correspond to almost rigid structures when compared to the spiral threads, mainly due to the higher stress levels of radial threads, representing little influence on the frequencies associated with local behavior induced by prey impact.

Thus, one may conclude that, for each region between two adjacent radial threads, the location of prey impact cannot be completely determined using the resonant frequency alone. Also, these results indicate a decoupling between the natural mode of vibration that may be generated by wind (Figure 4a, circa 16 Hz) and the frequency components associated with prey-induced vibration (>20 Hz), thus indicating robustness in prey detection.[43] Since the resonant frequencies are also dependent on the spiral thread stiffness and prey mass, this may possibly be used as an indicative of the size of prey.[44]

3.3. Vibration Transmission

We now apply force input signals, modeled as the function

$$f(t) = \begin{cases} A\,H_0(t)\,\sin(\omega_0 t), & 0 \le t \le T_0/2 \\ 0, & T_0/2 < t \le T \end{cases} \tag{3}$$

where $\omega_0 = 2\pi f_0$ is the circular frequency of the signal with fundamental frequency f_0, $T_0 = 1/f_0$, $H_0(t)$ is a smoothing function

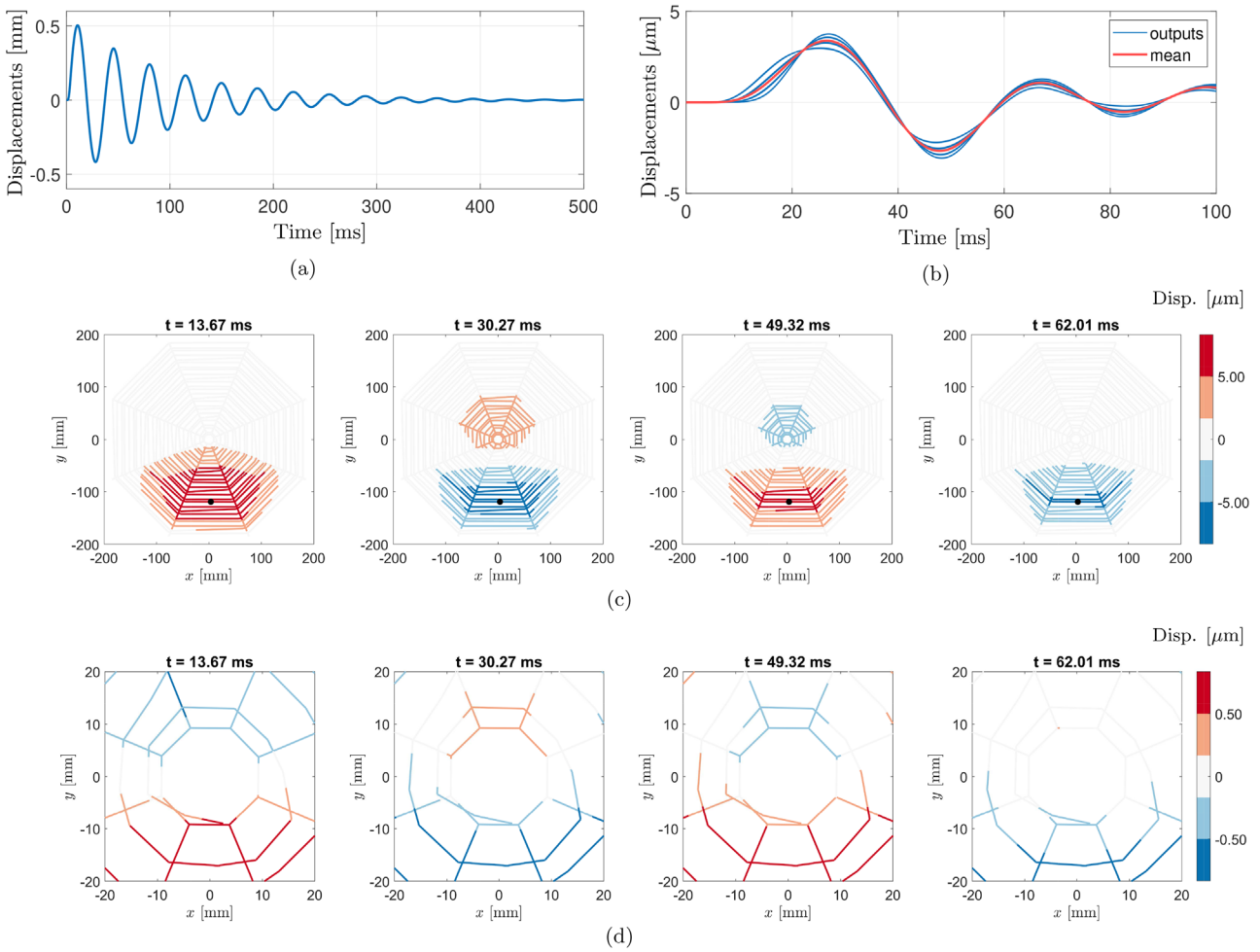

Figure 6. Computed transverse displacements considering an impact on an orb web with 100 MPa prestressed radial threads. a) The displacements of the input point resembles a damped mass-spring resonator. b) Output displacements present a similar behavior, with deviations with respect to their mean value. c) Displacement maps taken at different time instants indicate a wave-like propagation starting from the impact point, with opposing displacement signals at the region of the impact and the orb web center. d) Displacement maps relative to the orb web center. Color scale indicates transverse displacements in μm.

(Hanning window, used for a smoother transition from the initial zero value) of length T_0, and the constant A is defined so that the signal reaches a predefined maximum value. The value of T is chosen so as to allow a certain frequency resolution, given by $\Delta f = 1/T$.

For the computation of the following results, we consider a fundamental frequency of $f_0 = 100$ Hz (typical of insect impacts, see Section 1) and a maximum value of 10 μN. The actual duration of the input signal is of 5 ms ($T_0 = 10$ ms), which is considerably smaller than the period of the first bending modes of the spider orb web, and might thus be considered as an impulse signal. Also, the frequency content of this input signal is approximately zero for frequencies above 500 Hz.

For the case of linear vibration analyses, force inputs are applied at the same points (i.e., where prey masses are added) and the displacement response at the orb web center (defined here "output") is computed using a 1000 ms observation window (resolution frequency of 1 Hz).

3.3.1. Prey Localization Mechanism

Let us now consider displacements computed in 100 MPa prestressed radial threads, using a central impact point (represented using a black dot in Figure 5a). The computed input and output transverse displacements at the orb web center as a function of time and of the whole orb web at chosen time instants are shown in **Figure 6**.

The displacement of the input point, shown in Figure 6a, presents a characteristic damped frequency and decays to the equilibrium position, thus resembling a one degree-of-freedom damped mass-spring resonator with a first peak occurring at 10.7 ms. The displacements of the output points, shown in Figure 6b (with a restricted window of 100 ms for easier visualization) show their first peaks at ≈ 27.0 ms. The high speed of transverse wave propagation (in this case, 88 m s^{-1} for spiral and 277 m s^{-1} for radial threads, see Supporting Information) makes differences between different outputs small. Thus, to aid in their

Table 1. Comparison with literature values.

Spider species	Signal source	Time from prey impact to first response [s]	Ref.
Nephila clavipes	Electromagnetic vibrator	<0.040	[16]
Zygiella x-notata	Electromagnetic vibrator	<0.70	[17]
Nephila clavipes	Electromagnetic vibrator	<0.60	[17]
		0.055 (control)	
Leucauge mariana	*Drosophila melanogaster*	0.117 (3 radii cut)	[45]
		0.177 (all but 5 radii cut)	
	Agallia novella	0.0 (unfed), 0.2 (fed)	
Cyclosa turbinata	*Drosophila robusta*	0.5 (unfed), 0.4 (fed)	[44]
	Sitotroga cerealella	0.1 (unfed), 0.5 (fed)	
Araneus diadematus	*Drosophila* sp.	0.027	(Proposed model)

interpretation, we also indicate the instantaneous output displacement mean, $\overline{u}_{\text{out}}(t)$, given by

$$\overline{u}_{\text{out}}(t) = \frac{1}{N}\sum_{i=1}^{N} u_{\text{out}}^{(i)}(t) \tag{4}$$

where $u_{\text{out}}^{(i)}(t)$ is the out-of-plane displacement at the ith output node, computed considering all N output points. The deviation of the output points with respect to the instantaneous mean presents an inversion in their relative positions at 22.2 ms, thus indicating that the orb web center undergoes a wave-like movement, which may be indicative of the kind of stimulus that allows prey localization. This behavior is further analyzed considering the instantaneous displacement maps shown in Figure 6, which represents the orb web at a short time instant after the impact (13.7 ms) and close to the initial maximum and minimum values of the output displacements (30.2, 49.3, and 62.0 ms). Both the asymmetric displacement field profile displayed by the orb web and the opposite displacement signs between the impact region and the orb web center indicate an overall flexural mechanism of wave propagation.

It is also interesting to compare the time needed for vibrations to reach the orb web center to the values obtained from the literature (**Table 1**). The time intervals between the prey impact (or vibration caused by an electromagnetic source) and the first movements of spider legs present a large variation and depend on the spider species, the individual type of prey (or signal source), and structural conditions of the web. As a means of comparison, we consider the time that computed vibrations take to reach their maximum (around 27 ms). Thus, the time interval needed for information to reach the orb web center is in agreement with literature values, in particular.[16,45] It is important to note that this value is smaller in our case since in reality a delay is expected between the vibrations perceived by the spider and its neuromotor response, which is not considered in our numerical experiment.

Let us now restrict our investigation to the orb web center. Thus, we analyze the variations of the orb web center displacements with respect to their instantaneous mean value ($u_{\text{out}}^{(i)}(t) - \overline{u}_{\text{out}}(t)$, for each of the ith output nodes), as shown in Figure 6d. Soon after the impact (15.9 ms), the two radial threads adjacent to the spiral thread where the impact has occurred have the largest relative displacements, while the opposing two radial threads have the smallest relative displacements, thus indicating the impact direction. This behavior is observed in the following time instants, although with a smaller magnitude.

The correlation between the prey location and the displacements of the orb web center relative to its instantaneous mean value suggests the development of a metric capable of quantifying the improvement of prey sensitivity considering a given orb web configuration. We therefore define an energy-like metric, $E(t)$, which quantifies the energy associated with the inclination of the ith output node relative to the orb web center mean displacement, defined by

$$E_i(t) = \theta_i^2(t) \tag{5}$$

where $E_i(t)$ is the metric associated with the ith output node, and $\theta_i(t)$ is the inclination of this node, given by

$$\theta_i(t) = \tan^{-1}\left(\frac{u_{\text{out}}^{(i)}(t) - \overline{u}_{\text{out}}(t)}{L_{\text{spider}}}\right) \tag{6}$$

The normalization provided by the angular metric removes the contribution of the mean displacement, which presents no directional information (transverse mode in Figure 4a), while the energetic metric provides an absolute value associated with vibration energy in a given direction. Also, whenever output nodes have a similar displacement (flat web center), in which case no directional information is available, $u_{\text{out}}^{(i)}(t) \approx \overline{u}_{\text{out}}(t)$ for each $i = 1, \ldots, N$, which leads to $\theta_i(t) \approx 0$ and $E_i(t) \approx 0$. It is also important to note that the energy is not computed in an overall sense, as usually done in the literature, to account for the time-decay of vibrations due to damping mechanisms,[14] but instead, a novel metric designed to quantify a perceived level of energy at the orb web center is adopted. These metrics are illustrated in **Figure 7** and computed using data from Figure 6.

Figure 7a illustrates the normalized metric $\theta_i(t)$ computed for the output displacements following the numbering convention depicted Figure 7b, whose representative plot is shown in Figure 7c. These curves show a frequency close to 28.8 Hz, which corresponds to the frequency of the locally resonant transverse mode associated with the prey impact (see Figure 5b),

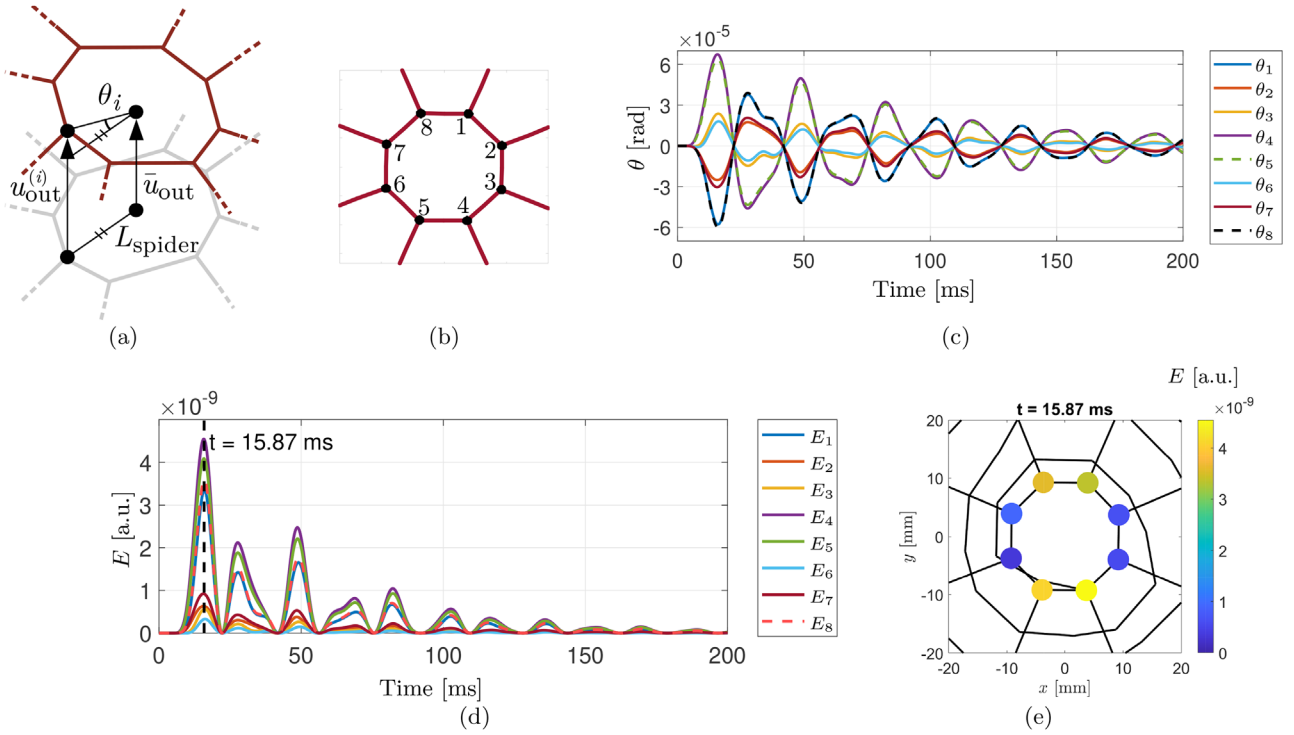

Figure 7. Angular and energetic metrics. a) The angle $\theta_i(t)$ is computed for the ith output node considering its out-of-plane displacement $u_{out}^{(i)}(t)$, the mean output displacement $\bar{u}_{out}(t)$ and the spider characteristic dimension L_{spider}. b) Orb web center (showing only radial threads) and output node numbering. c) Angular metric $\theta_i(t)$ and d) energy metric $E_i(t)$ computed for outputs points 1 through 8 e) Energy metric for output nodes at the time instant corresponding to its maximum.

suggesting it is sufficient to provide its directional information, acting as a continuous source of vibration, while the modes of the web itself (Figure 4) probably do not play a major role in this sense.

The energy metric $E_i(t)$ is also computed and shown in Figure 7d. The energy distribution at the central nodes for the time instant corresponding to its maximum value is shown in Figure 7e, indicating that the energy associated with the pair of output nodes corresponding to the radial threads closest to the impact region (4 and 5) present the largest values, while the opposing nodes (1 and 8) correspond to the two next largest values. We also note that the energy metric consistently indicates the pair of output nodes corresponding to the radial threads adjacent to the impact region ($E_4(t)$ and $E_5(t)$ in Figure 7d), thus providing a reliable indication for the source of vibration.

It is also interesting to notice that even though spiders possess a very complex and well developed sensing system,[39,46] these results suggest that monitoring the orb web center is sufficient to allow for the localization of prey. When considering only the two most energetic nodes, the precision of localization is probably limited by the spatial resolution of the orb web provided by the number of radial threads, in which case a larger number of radial threads provide a more accurate location.[16,45] This also indicates that the proposed energy metric can probably be used in the investigation of other phenomena associated with wave propagation in orb webs, which has not been done in the literature before. Henceforth, the envelope (maximum) of this metric will be used to quantify the perceived level of vibration at the orb web center.

3.3.2. Model Robustness

To assess the validity of the proposed metrics for varying web configurations, we perform the previous analyses considering orb webs obtained by i) doubling the number of radial threads, ii) doubling the radius of the orb web, and iii) increasing by 50% the mass density of the threads. For case i) the mass of the spider is considered distributed at every two nodes. The considered models, the maximum of the energy metric, and the energy computed for the output nodes at the time instant corresponding to its maximum are shown in **Figure 8**.

For the spider orb web with an increased number of radials (Figure 8a) the maximum of the energy metric (Figure 8b) presents a decrease in its period, which is associated with the shorter length of the spiral thread corresponding to the impact position, leading to an increased stiffness and corresponding resonance frequency. The energy distribution at the orb web center (Figure 8c) is still indicative of the direction of prey impact, also confirming that an increase in the number of radial threads may improve the localization accuracy.

For the spider orb web with a larger radius (Figure 8d), the maximum of the energy metric (Figure 8e) practically maintains its period, indicating that the frequency of vibration of the prey does not change, while also increasing its amplitude, which can be explained by a reduction in the stiffness of the orb web center, since it is now connected to longer radial threads. The corresponding maximum of the energy metric is shown for the output nodes (Figure 8f), correctly indicating the prey direction.

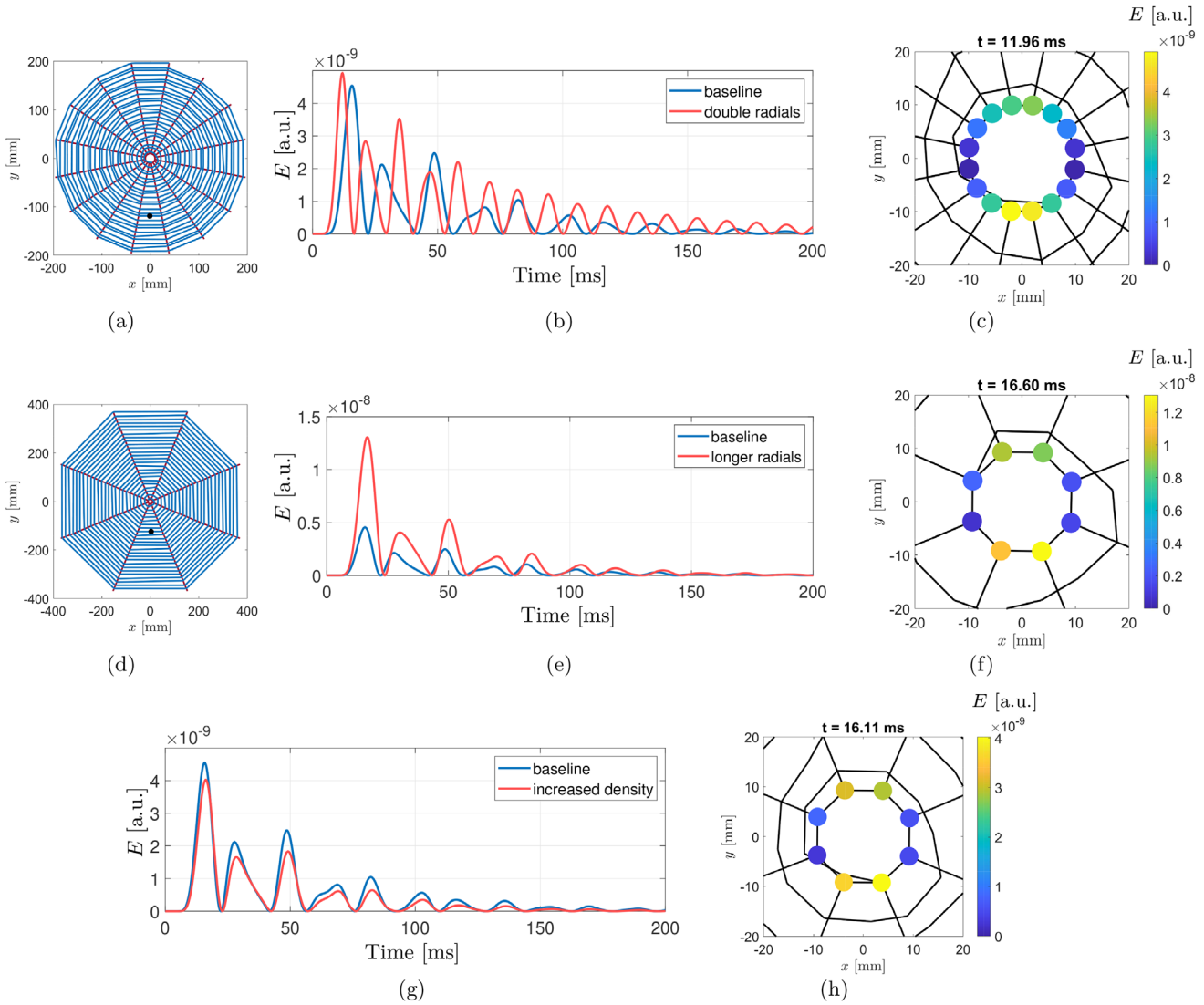

Figure 8. Computed results for varying orb web configurations. a) Orb web with increased number of radials, b) maximum of the energy metric, and c) corresponding energy computed at output nodes for web configuration in (a). d) Orb web with larger radius, e) maximum of the energy metric, and f) corresponding energy computed at output nodes for (d). For the case of threads with increased mass density, only the g) maximum of the energy metric and h) corresponding energy computed at output nodes are shown. In each case, the computed energy at the output nodes at the orb web center consistently indicate the prey impact position.

For the case of threads with an increased mass density, the maximum of the energy metric (Figure 8g) presents only negligible changes, which are associated with the decrease in the resonance frequency and rotation of the orb web center due to the increase in mass. The corresponding energy computed at the output nodes presents no noticeable changes (Figure 8h). Thus, these results show that the energy metric can be used with different spider orb web configurations to consistently indicate the location of prey vibration.

3.3.3. Angular Impact Point Variation

We now investigate the effects of varying the impact positions along a single spiral thread, starting from its central position and approaching one of its adjacent radial threads (**Figure 9**a) considering radial threads prestressed with 100 MPa.

Figure 9b shows an increase in the resonant frequencies (25–50 Hz region) of the local modes (as previously shown in Figure 5c) and a negligible effect on the first natural mode (15.8 Hz), which in fact does not aid in prey localization. Figure 9c shows that the energy computed at output nodes presents a noticeable increase for the input point CLK2, thus indicating that prey sensitivity is significantly improved near radial threads. This, in turn, again justifies that an increased number of radial threads may by highly beneficial to increase the orb web's efficiency in prey localization and retention. Also, distinct oscillation periods are associated with the corresponding locally resonant frequencies.

Figure 9d,f show the orb web transverse displacements following the impact at the points indicated by the black dots. The

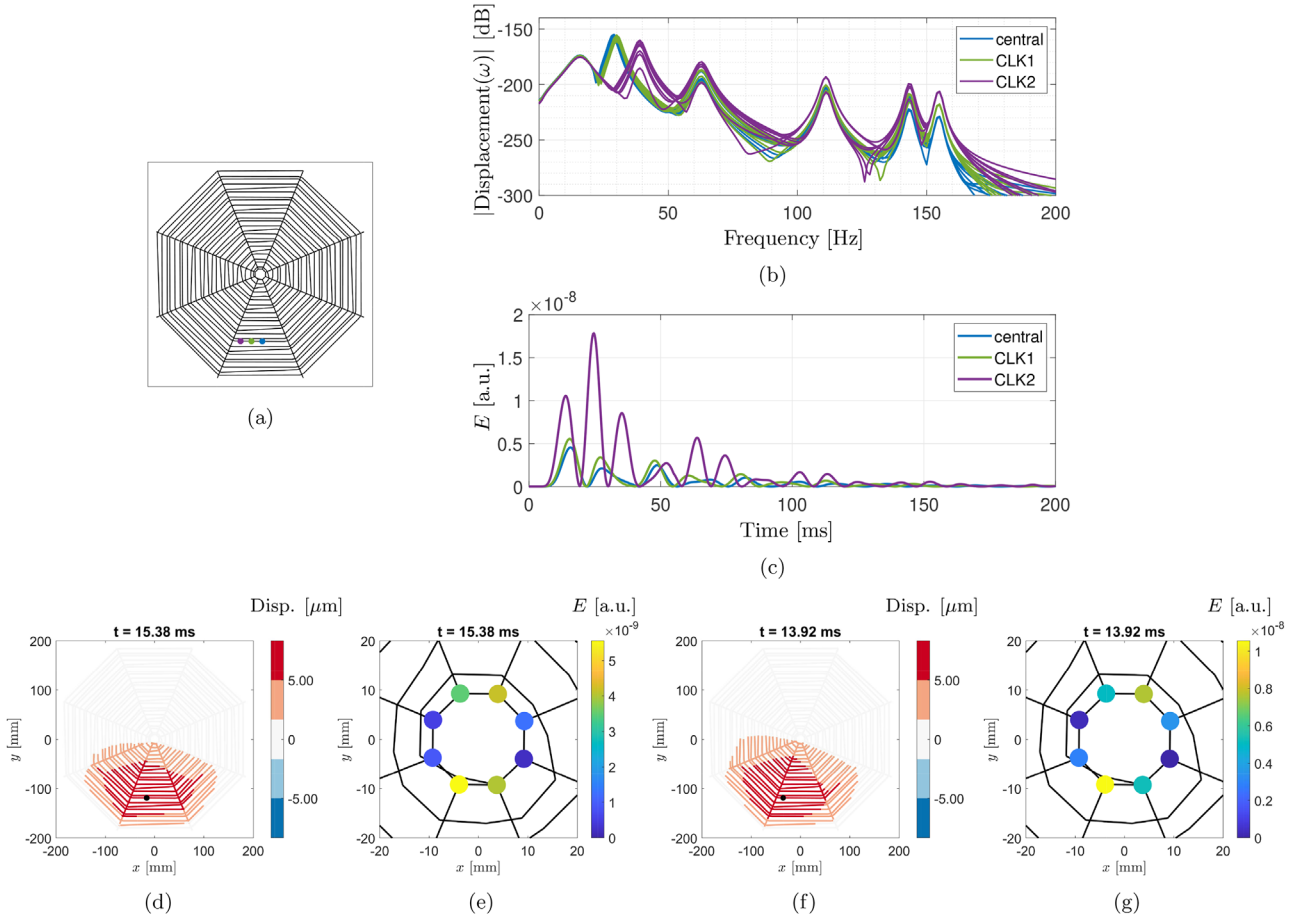

Figure 9. Effects of varying impact positions on a spiral thread. a) Input points are labeled as (●) central, (●) CLK1, and (●) CLK2. b) Frequency components of the output displacements show an increase in the resonant frequencies as the impact point approaches a connecting radial thread. c) The maximum energy computed at output nodes increases significantly closer to the radial threads. d) Transverse displacements of the orb web and e) energy computed at output nodes for impact position CLK1. f,g) Same as (d) and (e) for impact point CLK2.

variation of the impact point creates an asymmetric displacement profile involving the center of the corresponding spiral thread, thus suggesting it may be used by the spider to localize prey. Figure 9e,g show that the energy-like metric is able to capture the uneven energy distribution between output nodes even for slight changes in the impact positions, indicating that the output node corresponding to the radial thread closer to the impact contains most energy, followed by its corresponding opposing node.

3.3.4. Radial Impact Point Variation

Figure 10 presents the results computed considering impact points varying radially with 100 MPa prestressed radial threads.

Figure 10a indicates the considered impact points, varying in the radial direction. Figure 10b shows the additional resonance peaks introduced by local resonances (see Figure 5c) in the 25–50 Hz frequency range, which also implies an increase in their intensities, as also shown in Figure 10c considering the energy at the output nodes. Apart from the differences in intensities, no distinguishable features are noticed at the orb web center following the initial impact (Figure 10d,e).

It is interesting to notice that although local resonance mechanisms are a recurring feature in nature which may allow the discrimination between input signals,[47] our results indicate that frequency information alone cannot be used as a single source of information for position sensing, since an increase in the frequency of vibration may occur due to approximating i) an adjacent radial thread (along a spiral thread) or ii) the orb web center (along the radial orientation). Once again, these results indicate that an increased number of radial threads is beneficial for localizing prey, since it improves the orb web spatial resolution and consequently the likeliness of a radial thread being struck, thus leading the spider directly to prey.[45]

3.3.5. Stress Increase

Next, we briefly discuss the influence of the increased value of pre-stress in radial threads (150 MPa). Our results (not shown here for the sake of brevity) indicate that this increase has no detrimental effect on the frequency sensitivity of output displacements, while a shift in resonant frequencies not associated with the locally resonant vibration is also observed, which is due to the

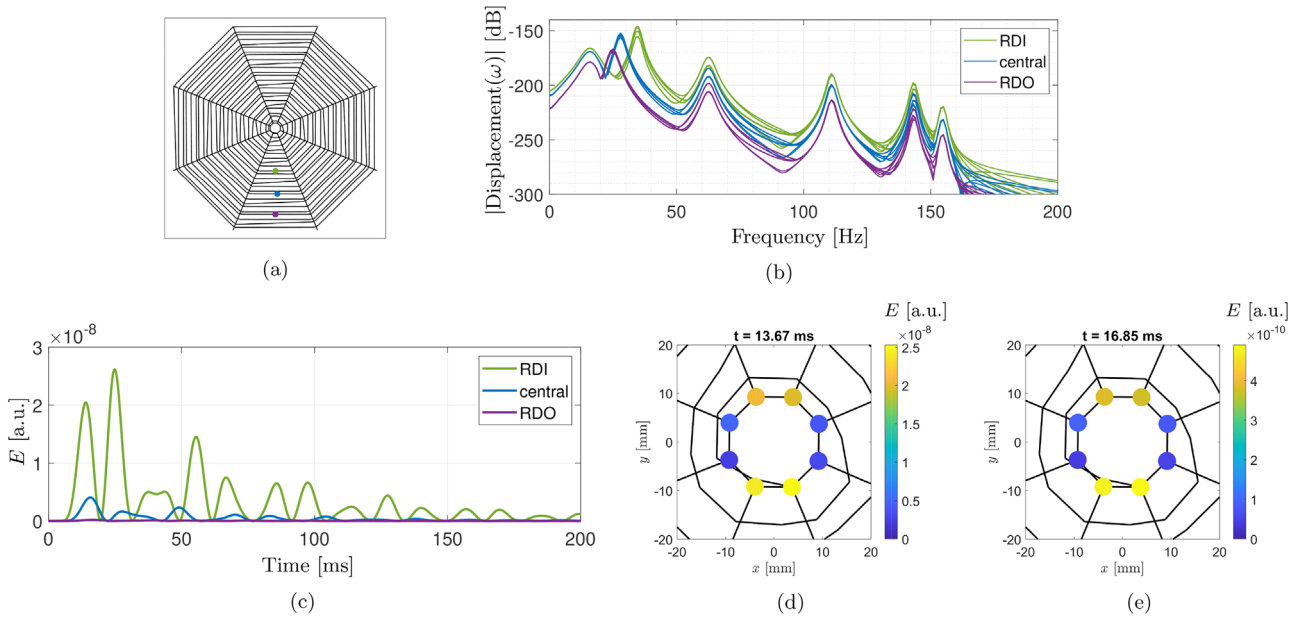

Figure 10. Effects of varying impact positions in the radial direction. a) Input points are labeled as (●) RDI, (●) central, and (●) RDO. b) Frequency components of the output displacements show an increase in the resonant frequencies as the impact point approaches the orb web center. c) The maximum energy following the impact decreases as the impact points is located farther from the orb web center. The energy distributions at the output nodes d) RDI and e) RDO present no distinguishable features apart from absolute values.

increase in the system stiffness. This increase in stiffness also leads to a smaller level of relative displacements at the orb web center, thus implying a smaller level of energy according to our proposed metric, but also a smaller time delay needed to reach the peak value. The increase in the speed of transverse waves increases is caused by the increase in stresses (see Supporting Information), which may be important for the spider's overall preying behavior. This is also supported by the fact that different mechanisms may take place in tuning the threads stresses, such as supercontraction.[24]

3.3.6. Influence of Mooring Threads

Our current spider orb web model considers rigid connections at the outer edges of radial threads. However, the presence of mooring and frame threads is a common trait that nearly always breaks the geometrical symmetry in real orb webs and has been shown to have a fundamental role in their structural behavior.[48]

As the design of these framing structures may greatly vary, here we present results obtained considering a simple model as an octagon in which the initial Archimedean spiral is inscribed, connected to four anchoring nodes. Each vertex of the initial octagon and anchoring nodes are then shifted in both x and y directions according to a random variable distribution in the range [0, 50] mm, while the spiral is limited to the shortest connection between the radials and the framing threads, as shown in **Figure 11**a. The frame and mooring threads (shown in green in the figure) have the same material properties as the radial threads, but with a radius of 5.0 μm.[20] The natural modes corresponding to the transverse displacement and bending modes (see Figure 4), the energy metric computed at the output nodes, and its representation at maxima points are shown in Figure 11.

The inclusion of mooring and frame threads can significantly change both the mode shapes and resonant frequencies of the orb web, most notably leading to the breaking of symmetry when considering the bending modes resonant frequencies (Figure 11b–d). However, the resonant mode and frequency associated with the prey vibration remains practically unchanged (Figure 11e). Likewise, the use of the energy metric (Figure 11f) is still able to identify the prey direction, since the output node 4 is the most energetic, while its adjacent node 5 is more energetic than node 3, which is also illustrated at the output nodes at the time instant corresponding to the maximum energy (Figure 11g,h). This suggests that the proposed metric is probably unaffected by variations in the attachment conditions of the orb web, due to its locally resonant mechanism, mainly influenced by the local stiffness and mass characteristics of the spiral thread where the prey is located and its adjacent radial threads.

3.3.7. Nonlinearity Effects

We now investigate the effects of nonlinear material properties in wave propagation considering varying input force intensities. We consider the same central impact point indicated in Figure 5a, restricting our analysis to a 50 ms time window to assess the effects of the increase of amplitude. The computed maximum input displacements for 10, 500, and 1000 μN are, respectively, 0.53, 24.7, and 44.3 mm, thus indicating the effects of nonlinearity.

The energy computed at the orb web center outputs (with the angular metric $\theta(t)$ normalized to account for each input value,

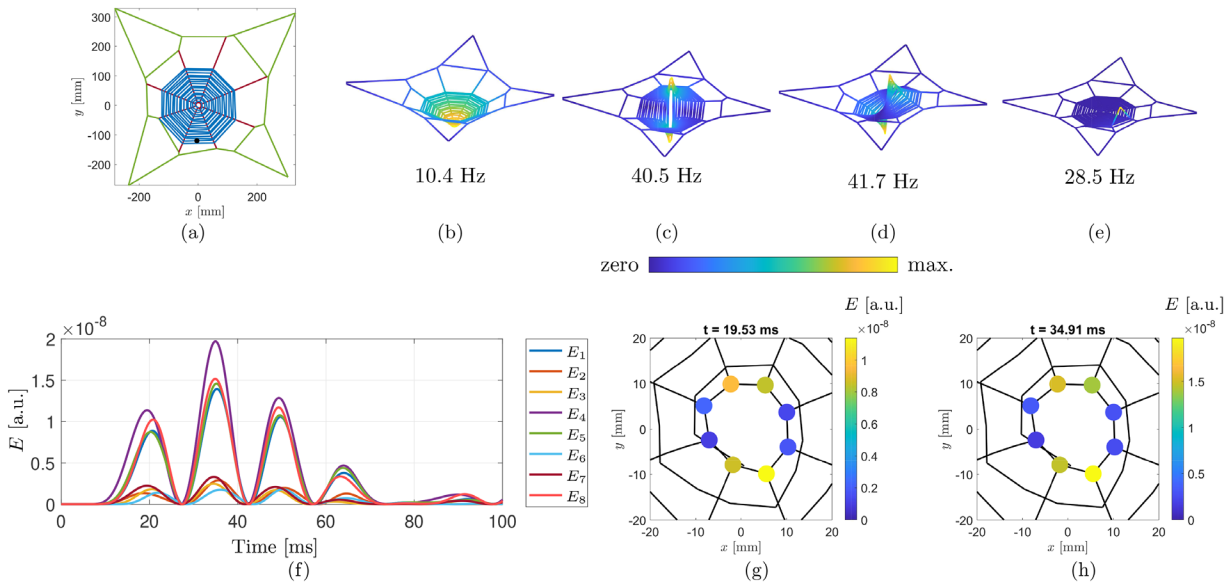

Figure 11. Results computed considering a simple model for mooring threads. a) Orb web including mooring and frame threads (green lines). The transverse displacement and bending vibration modes considering the orb web and spider mass b,c,d) presents a large variation when compared to the configuration without mooring threads, while e) the resonant mode associated with the inclusion of prey does not change significantly. The energy metric f) is consistent in indicating the prey location, which is also shown for the output nodes at the first two time instants that present g,h) maximum energy.

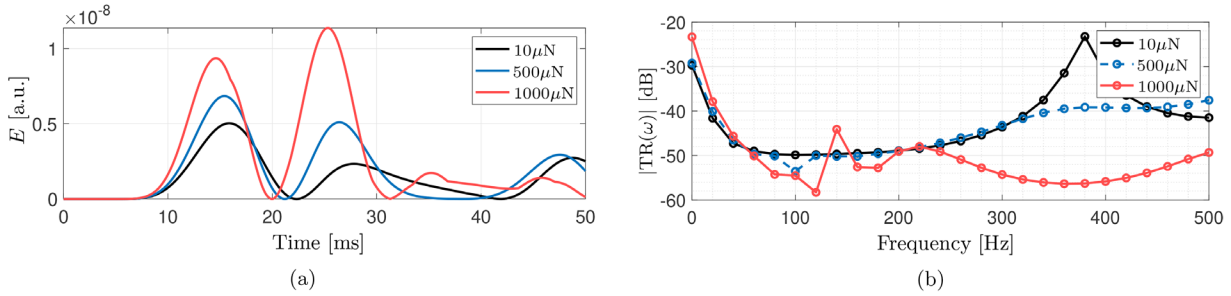

Figure 12. Effects of material nonlinearity. a) The effects of nonlinearity on the energy at the orb web center output nodes substantially increase for sufficiently large force values. b) For sufficiently large force values, the frequency response presents a larger decrease up to 120 Hz, after which it maintains a relatively uniform response up to 500 Hz.

that is, 1/50 for the 500 μN and 1/100 for the 1000 μN input forces) and the displacement transmissibility (TR(ω), computed considering the frequency components of the mean output displacements, $\hat{\bar{u}}_{\text{out}}(\omega)$, and input displacements, $\hat{u}_{\text{in}}(\omega)$, as $\text{TR}(\omega) = \hat{\bar{u}}_{\text{out}}(\omega)/\hat{u}_{\text{in}}(\omega)$) are shown in **Figure 12**.

Figure 12a shows that the nonlinear material behavior can both proportionally increase the energy at the orb web center output nodes and decrease the time to peak response, thus providing a twofold positive effect and improve the prey sensing behavior. Also, it is possible to notice a change in the orb web filtering capability, as shown in Figure 12b. The increase in the input force produces a monotonic decrease up to 120 Hz, while above 140 Hz, the response remains somewhat constant. It also shows an enhancement in frequencies below 40 Hz, thus indicating an improvement in sensitivity at lower frequencies, which are associated with prey vibration local resonances (see Figure 5). The locations of prey impacts associated to lower resonant frequencies also have lower output energies at the orb web center (see Figures 9 and 10). Thus, the resulting transmissibility curve also suggests the enhancing of sensitivity at frequencies which present lower energy output.

3.4. Prey Location Estimation

The question of whether the prey direction can be properly estimated by the spider using instantaneous information obtained from the vibration at the orb web center is fundamental.[16] It is important to note that vibration sensing is only one of the prey localization methods employed by spiders since several other senses such as high angular vision[49] and olfaction[50] are also used, thus creating a multi-sensory prey detection system. To this end, we propose a metric to estimate the direction of the vibration source due to prey impact. We denote such metric by $\overline{\psi}$, which is given by

$$\overline{\psi}(t) = \frac{E_p(t)\psi_p + E_q(t)\psi_q}{E_p(t) + E_q(t)} \tag{7}$$

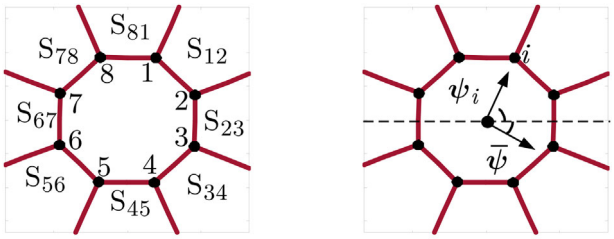

Figure 13. Quantities used in prey location estimation. a) Sections defined as regions between two adjacent output nodes and their corresponding radial threads. b) Heading angle associated with the ith output node, ψ_i, and estimated heading angle, $\overline{\psi}$.

where ψ_i and $E_i(t)$ are the heading angle and the energy (see Equation (5)) of the ith output node. Indexes p and q are the ones that maximize the energy-like function given by

$$S_{ij}(t) = E_i(t) + E_j(t) \tag{8}$$

which represents the combined energy of output nodes at the orb web center, thus indicating the region which most likely contains the source of energy. Such concepts are illustrated in **Figure 13**. Although some time intervals may present small levels of overall computed output energy (instants with θ very close to zero, see Figure 7c,d), soon after the impact the output energy presents considerable levels, which makes it a reliable metric.

The results computed using the direction estimation metric given in Equation (7) considering different impact positions (Figures 9a and 10a) are shown in **Figure 14** restricted to 0–50 ms for better visualization. We also present the maximum of the energy per section (metric given in Equation (8)) and the relative errors between the estimated direction and the actual prey location direction.

Figure 14 shows that the proposed metric is consistent in estimating the actual direction of prey impact. The metric fails at very small values of output node energies, which indicate almost zero differences in transverse displacements at the orb web center and therefore present no relevant directional information. In the remaining time intervals, the error in the estimated angles is generally kept below 5%. The worst result is observed for an impact point very close to a radial thread, which implies in a source of vibration with a higher frequency, thus yielding a larger number of time intervals with small energy levels.

These results suggest that even with a small number of radial threads (compared to much larger numbers reported in the literature[16]), it may be possible for the spider to localize prey with considerable precision. This observation is also in agreement with the literature, where a small number of radial threads is shown to be sufficient for the spider to monitor prey.[45] This also indicates that an increase in the number of radial threads are not strictly necessary for prey localization, although it is certainly beneficial, especially for prey retention and for dissipation of energy.[14]

4. Concluding Remarks

In conclusion, we have numerically analysed the prey detection mechanism in a spider orb web. The presence of the prey does not affect the existing modes of vibration of the system constituted by the spider and orb web, most noticeably introducing locally resonant modes. The frequencies of these modes increase as the prey impact position approaches the orb web center or radial threads, and are thus probably not sufficient to indicate prey location.

The prey vibration continuously transmits energy to the radial threads and allows detection at the corresponding nodes at the orb web center, which is asymmetrically distributed toward the direction of the vibration source. To quantify this behavior, we have proposed a metric to compute the perceived energy at the

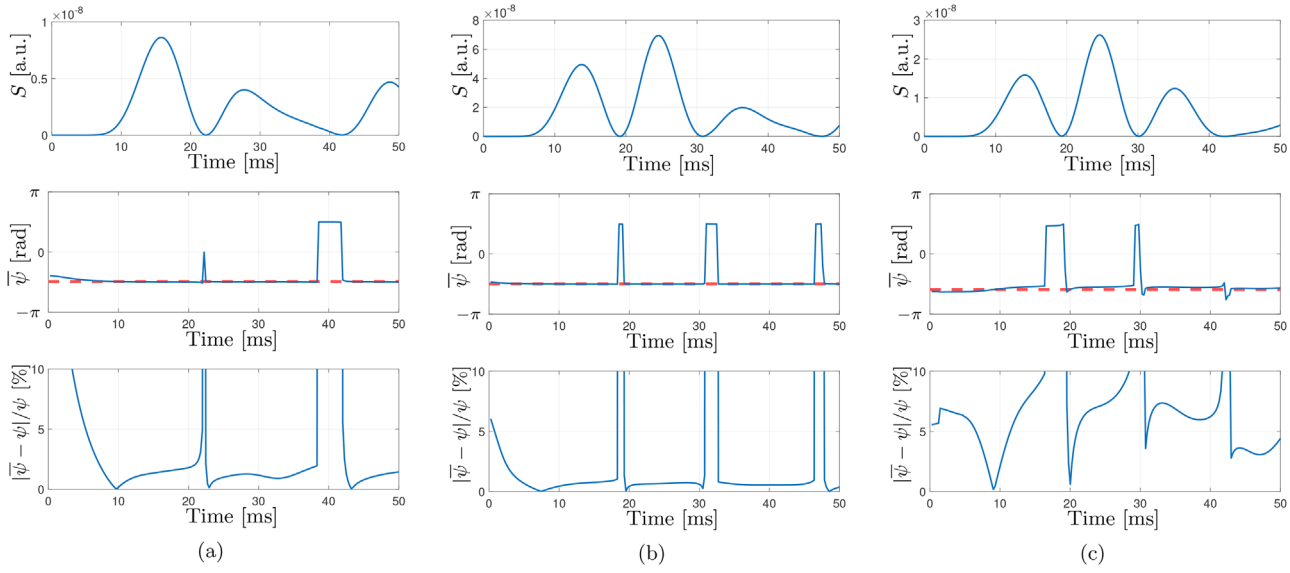

Figure 14. Maximum energy per sector, estimated prey direction (- - indicates actual prey location), and corresponding relative errors for a) central, b) RDI, and c) CLK2 impact points.

orb web center, which can be used to consistently determine the region between radial threads that contains the vibration source, also discriminating angular variations. The proposed metric can consistently indicate the radial threads that are excited by prey impact also when considering different orb web configurations, including variations in the number of radial threads, length of the radial threads, mass density, and the presence of mooring and frame threads. We have also demonstrated, through a proposed angle estimation approach, that a large number of radial threads are not strictly necessary for the angular localization of prey, although an increase in their number may be beneficial, especially in the radial direction.

We have also shown that an increase in the prestress value of radial threads decreases the rotation of the orb web center toward a given vibration source direction, while also decreasing the time to peak response due to stress stiffening. Most notably, the effects of material nonlinearity are shown to produce a twofold effect, both increasing the maximum energy at the orb web center and decreasing the time to reach peak values, consequently improving prey localization.

The functioning of prey sensing based on locally resonant mechanisms and the proposed metrics of energy outputs at the orb web center and prey location estimation are thus presented as new paradigms, which may be used for the analysis of spider behavior and in the development of novel sensing technologies based on spider web-like structures.

Supporting Information

Supporting Information is available from the Wiley Online Library or from the author.

Acknowledgements

VFDP, FB, and NMP are supported by the EU H2020 FET Open "Boheme" grant No. 863179. GG is supported by Caritro Foundation (prot. U1277.2020/SG.1130).

Conflict of Interest

The authors declare no conflict of interest.

Data Availability Statement

The data that support the findings of this study are available from the corresponding author upon reasonable request.

Keywords

finite element method, orb web, spider, vibrations, waves

Received: July 28, 2021
Revised: November 25, 2021
Published online:

[1] W. Eberhard, *Spider Webs: Behavior, Function, and Evolution*, University of Chicago Press, Chicago, IL **2020**.
[2] G. Greco, V. Mastellari, C. Holland, N. M. Pugno, *Perspect. Sci.* **2021**, *29*, 133.
[3] F. Vollrath, P. Selden, *Annu. Rev. Ecol., Evol., Syst.* **2007**, *38*, 819.
[4] G. Greco, N. M. Pugno, *J. R. Soc. Interface* **2021**, *18*, 20200907.
[5] W. M. Masters, H. Markl, *Science* **1981**, *213*, 363.
[6] M. Miniaci, A. Krushynska, A. B. Movchan, F. Bosia, N. M. Pugno, *Appl. Phys. Lett.* **2016**, *109*, 071905.
[7] A. O. Krushynska, F. Bosia, M. Miniaci, N. M. Pugno, *New J. Phys.* **2017**, *19*, 105001.
[8] S. Sepehri, H. Jafari, M. M. Mashhadi, M. R. H. Yazdi, M. M. S. Fakhrabadi, *Int. J. Solids Struct.* **2020**, *204*, 81.
[9] H. Huang, E. Cao, M. Zhao, S. Alamri, B. Li, *Polymers* **2021**, *13*, 1146.
[10] S. W. Cranford, A. Tarakanova, N. M. Pugno, M. J. Buehler, *Nature* **2012**, *482*, 72.
[11] R. V. Lewis, *Chem. Rev.* **2006**, *106*, 3762.
[12] L. Eisoldt, A. Smith, T. Scheibel, *Mater. Today* **2011**, *14*, 80.
[13] G. Greco, M. F. Pantano, B. Mazzolai, N. M. Pugno, *Sci. Rep.* **2019**, *9*, 5776.
[14] A. T. Sensenig, K. A. Lorentz, S. P. Kelly, T. A. Blackledge, *J. R. Soc. Interface* **2012**, *9*, 1880.
[15] W. M. Masters, *Behav. Ecol. Sociobiol.* **1984**, *15*, 207.
[16] M. A. Landolfa, F. G. Barth, *J. Comp. Phys. A* **1996**, *179*, 493.
[17] D. Klärner, F. G. Barth, *J. Comp. Phys.* **1982**, *148*, 445.
[18] B. Mortimer, *Integr. Comp. Biol.* **2019**, *59*, 1636.
[19] T. Watanabe, *Proc. R. Soc. Lond., Ser. B: Biol. Sci.* **2000**, *267*, 565.
[20] B. Mortimer, A. Soler, C. R. Siviour, R. Zaera, F. Vollrath, *J. R. Soc. Interface* **2016**, *13*, 20160341.
[21] I. G. Main, *Vibrations and Waves in Physics*, Cambridge University Press, Cambridge **1993**.
[22] E. Wirth, F. G. Barth, *J. Comp. Phys. A* **1992**, *171*, 359.
[23] C. Boutry, T. A. Blackledge, *J. Exp. Biol.* **2010**, *213*, 3505.
[24] C. Boutry, T. A. Blackledge, *J. Exp. Biol.* **2013**, *216*, 3606.
[25] S. Kaewunruen, C. Ngamkhanong, T. Yang, *Appl. Sci.* **2020**, *10*, 6032.
[26] A. A. Rhisiart, F. Vollrath, *Behav. Ecol.* **1994**, *5*, 280.
[27] S. Zschokke, F. Vollrath, *Ekológia (Bratislava, Slovakia)* **2000**, *19*, 307.
[28] G. Greco, J. O. Wolff, N. M. Pugno, *Front. Mater.* **2020**, *7*, 138.
[29] J. Jyoti, A. Kumar, P. Lakhani, N. Kumar, B. Bhushan, *Philos. Trans. R. Soc. A* **2019**, *377*, 20180271.
[30] B. Mortimer, C. Holland, J. F. C. Windmill, F. Vollrath, *J. R. Soc. Interface* **2015**, *12*, 20150633.
[31] B. Mortimer, A. Soler, C. R. Siviour, F. Vollrath, *Sci. Nat.* **2018**, *105*, 37.
[32] R. Jocqué, *Biol. Jaarb.* **1981**, *49*, 155.
[33] M. Denny, *J. Exp. Biol.* **1976**, *65*, 483.
[34] A. Brandwood, *J. Exp. Biol.* **1985**, *116*, 141.
[35] A. T. Sensenig, I. Agnarsson, T. A. Blackledge, *J. Zool.* **2011**, *285*, 28.
[36] H. Frings, M. Frings, *Ecology* **1966**, *47*, 578.
[37] F. G. Barth, U. Wastl, J. A. C. Humphrey, R. Devarakonda, *Philos. Trans. R. Soc. Lond., Ser. B: Biol. Sci.* **1993**, *340*, 445.
[38] B. Cummins, T. Gedeon, I. Klapper, R. Cortez, *J. Theor. Biol.* **2007**, *247*, 266.
[39] F. G. .Barth,*Zoology* **2002**, *105*, 271.
[40] S. L. Young, M. Chyasnavichyus, M. Erko, F. G. Barth, P. Fratzl, I. Zlotnikov, Y. Politi, V. V. Tsukruk, *Acta biomater.* **2014**, *10*, 4832.
[41] C. A. Clerck, *Svenska Spindlar*, Salvius, Stockholm **1757**.
[42] W. B. Worthen, *Evolution* **1996**, 2523.
[43] J. Turner, F. Vollrath, T. Hesselberg, *Sci. Nat.* **2011**, *98*, 1063.
[44] R. B. Suter, *Behav. Ecol. Sociobiol.* **1978**, 283.
[45] R. D. Briceño, W. G. Eberhard, *J. Arachnol.* **2011**, *39*, 102.
[46] F. G. Barth, *A Spider's World: Senses and Behavior*, Springer, Berlin, Heidelberg **2002**.
[47] T. Reichenbach, A. J. Hudspeth, *Rep. Progress Phys.* **2014**, *77*, 076601.
[48] A. Soler, R. Zaera, *Sci. Rep.* **2016**, *6*, 31265.
[49] N. I. Morehouse, E. K. Buschbeck, D. B. Zurek, M. Steck, M. L. Porter, *Biol. Bull.* **2017**, *233*, 21.
[50] S. Hostettler, W. Nentwig, *Funct. Ecol.* **2006**, *20*, 369.

Prey Impact Localization Enabled by Material and Structural Interaction in Spider Orb Webs (Supporting Information)

Vinícius F. Dal Poggetto Federico Bosia Gabriele Greco Nicola M. Pugno**

V. F. Dal Poggetto
Laboratory for Bioinspired, Bionic, Nano, Meta Materials & Mechanics, Department of Civil, Environmental and Mechanical Engineering, University of Trento, 38123 Trento, Italy
Email Address: v.fonsecadalpoggetto@unitn.it

F. Bosia
DISAT, Politecnico di Torino, 10129 Torino, Italy

G. Greco
Laboratory for Bioinspired, Bionic, Nano, Meta Materials & Mechanics, Department of Civil, Environmental and Mechanical Engineering, University of Trento, 38123 Trento, Italy

N. M. Pugno
Laboratory for Bioinspired, Bionic, Nano, Meta Materials & Mechanics, Department of Civil, Environmental and Mechanical Engineering, University of Trento, 38123 Trento, Italy
School of Engineering and Materials Science, Queen Mary University of London, Mile End Road, London E1 4NS, United Kingdom
Email Address: nicola.pugno@unitn.it

1 Thread properties

The modeling of both dragline and viscid silks are directly taken from the empirically parameterized data presented by Cranford et al. [1], corresponding to threads of the species *Araneus diadematus*. Dragline silk threads have stress-strain relations modeled using the relation

$$\sigma_d(\varepsilon) = \begin{cases} E_1\varepsilon & , \quad 0 \leq \varepsilon < \varepsilon_y\,, \\ e^{\alpha(\varepsilon-\varepsilon_y)} + \beta(\varepsilon-\varepsilon_y) + C_1 & , \quad \varepsilon_y \leq \varepsilon < \varepsilon_s\,, \\ E_2(\varepsilon-\varepsilon_s) + C_2 & , \quad \varepsilon_s \leq \varepsilon < \varepsilon_b\,, \\ 0 & , \quad \varepsilon \geq \varepsilon_b\,, \end{cases} \tag{1}$$

where the strain ε is given by $\varepsilon(L) = (L-L_0)/L_0$, L_0 is the initial thread length and L is the final thread length, E_1 is the thread initial stiffness, α is an exponential parameter, β is a tangent stiffness parameter, E_2 is the final stiffness, and the limits of distinct strain regions are given by the yielding strain ε_y, the softening strain ε_s, and the ultimate strain ε_b. Numerical values of these parameters are given by $E_1 = 10,000$ MPa, $\alpha = 43.1$, $\beta = 1,000$ MPa, $E_2 = 2,087.4$ MPa, $\varepsilon_y = 0.02$, $\varepsilon_s = 0.17$, and $\varepsilon_b = 0.27$. Constants C_1 and C_2 ensure the continuity between distinct regions and are given by $C_1 = E_1\varepsilon_y - 1$ and $C_2 = e^{\alpha(\varepsilon_s-\varepsilon_y)} + \beta(\varepsilon_s-\varepsilon_y) + C_1$.
Viscid threads are modeled by the stress-strain relation

$$\sigma_v(\varepsilon) = ae^{\varepsilon} + b\varepsilon + c\,, \tag{2}$$

where a is an exponential parameter, b is a tangent stiffness parameter, and c is a continuity constant. Numerical values of these parameters are given by $a = 44$ MPa, $b = -41$ MPa, and $c = -44$ MPa. The validity of this model lies in the range $0 \leq \varepsilon < 2.7$, which corresponds to the ultimate stress $\sigma_b = 500$ MPa. The resulting stress-strain relations for both dragline and viscid threads are presented in **Figure 1**.
Another important property is the tangential Young's modulus, which can be obtained for each type of thread by the relation $E_t = \frac{d\sigma}{d\varepsilon}$, which remains valid for each specific strain region, but presents discontinuities at the transition strains (ε_y, ε_s, and ε_b).

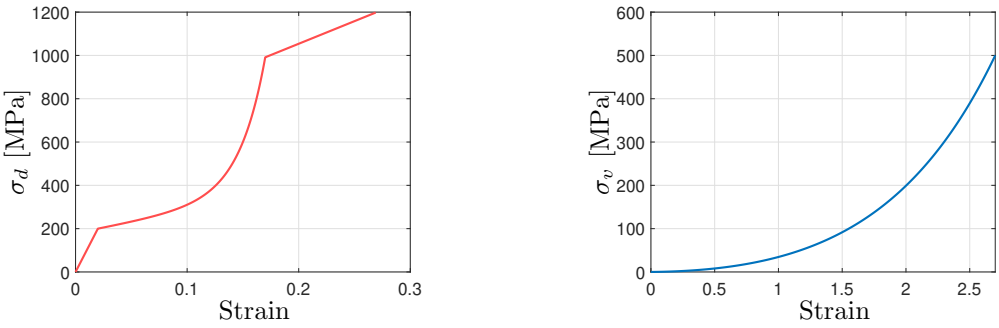

(a) (b)

Figure 1: Stress-strain relations for (a) (–) dragline and (b) (–) viscid threads.

2 Continuum mechanics definitions

2.1 Strain energy

Consider an infinitesimal element undergoing a displacement field $\mathbf{u} = \begin{Bmatrix} u_x & u_y & u_z \end{Bmatrix}^T$ using a Cartesian coordinate system. The Green-Lagrange strain associated with displacements ($\overline{\varepsilon}$) of one-dimensional elements undergoing general three-dimensional displacements is given by [2]

$$\overline{\varepsilon} = \frac{\partial u_x}{\partial x} + \frac{1}{2}\left[\left(\frac{\partial u_x}{\partial x}\right)^2 + \left(\frac{\partial u_y}{\partial x}\right)^2 + \left(\frac{\partial u_z}{\partial x}\right)^2\right]. \tag{3}$$

Assume a generic stress-strain relation given by $\sigma = \sigma(\varepsilon)$, and a given equilibrium state (ε_0, σ_0). Additional displacements applied with respect to this initial strain ε_0 induce additional strains, denoted here as $\Delta\varepsilon$, which imply in an additional strain energy density (per unit volume) U_0, given by

$$U_0 = \int_{\varepsilon_0}^{\varepsilon_0+\Delta\varepsilon} \sigma(\varepsilon)\, d\varepsilon\,. \tag{4}$$

It is important to stress out that this term does not represent all of the medium stored elastic energy (which was previously stressed at the equilibrium state), but rather an energy increment.
Considering the tangential Young's modulus E_t, given by

$$E_t = \left[\frac{d\sigma}{d\varepsilon}\right]_{\varepsilon=\varepsilon_0}, \tag{5}$$

the variation in stress $\Delta\sigma$ can be approximated using

$$\Delta\sigma = E_t \Delta\varepsilon\,. \tag{6}$$

Thus, the additional strain energy can be approximated by $\overline{U}_0$, yielding

$$U_0 \approx \overline{U}_0 = \sigma_0\Delta\varepsilon + \frac{1}{2}\Delta\varepsilon\,\Delta\sigma = \sigma_0\Delta\varepsilon + \frac{1}{2}E_t\Delta\varepsilon^2\,. \tag{7}$$

These concepts are illustrated in **Figure** 2.
The additional strain is caused by the displacements of elements measured with respect to the state equilibrium (i.e., displacements are zero at ε_0), which means that these are suitably substituted by the expression given in Eq. (3) (i.e., $\Delta\varepsilon = \overline{\varepsilon}$), yielding

$$\begin{aligned}\overline{U}_0 = \sigma_0 &\left\{\frac{\partial u_x}{\partial x} + \frac{1}{2}\left[\left(\frac{\partial u_x}{\partial x}\right)^2 + \left(\frac{\partial u_y}{\partial x}\right)^2 + \left(\frac{\partial u_z}{\partial x}\right)^2\right]\right\} + \\ &\frac{1}{2}E_t\left\{\frac{\partial u_x}{\partial x} + \frac{1}{2}\left[\left(\frac{\partial u_x}{\partial x}\right)^2 + \left(\frac{\partial u_y}{\partial x}\right)^2 + \left(\frac{\partial u_z}{\partial x}\right)^2\right]\right\}^2,\end{aligned} \tag{8}$$

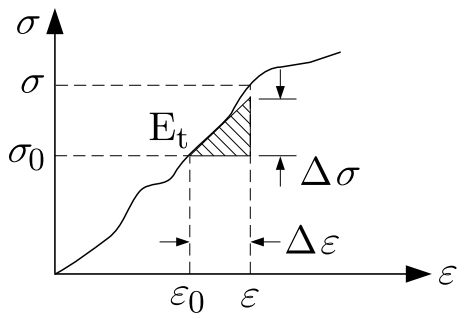

Figure 2: Stress-strain relation given by $\sigma = \sigma(\varepsilon)$. Starting from an equilibrium state $(\varepsilon_0, \sigma_0)$, an additional strain energy density is associated with additional strains $\Delta\varepsilon$, which can be related to an approximate increase in stresses σ using $\Delta\sigma = E_t\Delta\varepsilon$, with E_t being the tangential Young's modulus at $(\varepsilon_0, \sigma_0)$.

which can be approximated, considering terms up to $O(x^2)$, yielding

$$\overline{U}_0 \approx \sigma_0 \frac{\partial u_x}{\partial x} + \frac{1}{2}\sigma_0 \left[\left(\frac{\partial u_x}{\partial x} \right)^2 + \left(\frac{\partial u_y}{\partial x} \right)^2 + \left(\frac{\partial u_z}{\partial x} \right)^2 \right] + \frac{1}{2} E_t \left(\frac{\partial u_x}{\partial x} \right)^2 . \tag{9}$$

3 Finite element definitions

3.1 Stiffness and mass matrix

In the case of a two-node isoparametric finite element with length L and linear interpolation functions [3], if one considers element nodes i and j, the displacement field can be interpolated as

$$u_p(x) = \left(1 - \frac{x}{L}\right) u_{pi} + \frac{x}{L} u_{pj} \tag{10}$$

where $p = \{x, y, z\}$, which can be summarized in matrix notation as

$$\mathbf{u} = \mathbf{N}\mathbf{u}_e \,, \tag{11}$$

where $\mathbf{u}$ the interpolated displacements, $\mathbf{N}$ is an interpolating matrix, and $\mathbf{u}_e$ are the nodal displacements, given respectively by

$$\begin{aligned} \mathbf{u} &= \begin{Bmatrix} u_x & u_y & u_z \end{Bmatrix}^T , \\ \mathbf{N} &= \begin{bmatrix} 1-\frac{x}{L} & 0 & 0 & \frac{x}{L} & 0 & 0 \\ 0 & 1-\frac{x}{L} & 0 & 0 & \frac{x}{L} & 0 \\ 0 & 0 & 1-\frac{x}{L} & 0 & 0 & \frac{x}{L} \end{bmatrix} = \begin{bmatrix} (1-\frac{x}{L})\mathbf{I}_3 & \frac{x}{L}\mathbf{I}_3 \end{bmatrix} , \\ \mathbf{u}_e &= \begin{Bmatrix} u_{xi} & u_{yi} & u_{zi} & u_{xj} & u_{yj} & u_{zj} \end{Bmatrix}^T , \end{aligned} \tag{12}$$

where $\mathbf{I}_3$ is the order 3 identity matrix.
The strain vector $\boldsymbol{\varepsilon}$ can also be written using nodal displacements as

$$\boldsymbol{\varepsilon} = \begin{Bmatrix} \frac{\partial u_x}{\partial x} \\ \frac{\partial u_y}{\partial x} \\ \frac{\partial u_z}{\partial x} \end{Bmatrix} = \frac{\partial}{\partial x} \begin{Bmatrix} u_x \\ u_y \\ u_z \end{Bmatrix} = \frac{\partial}{\partial x} \mathbf{N}\mathbf{u}_e = \mathbf{B}\mathbf{u}_e \,, \tag{13}$$

where the strain-displacement matrix $\mathbf{B}$ is given by

$$\mathbf{B} = \begin{bmatrix} -\frac{1}{L} & 0 & 0 & \frac{1}{L} & 0 & 0 \\ 0 & -\frac{1}{L} & 0 & 0 & \frac{1}{L} & 0 \\ 0 & 0 & -\frac{1}{L} & 0 & 0 & \frac{1}{L} \end{bmatrix} = \begin{bmatrix} -\frac{1}{L}\mathbf{I}_3 & \frac{1}{L}\mathbf{I}_3 \end{bmatrix} . \tag{14}$$

The increase in strain energy density given by Eq. (9) can be written in matrix notation by first rewriting as

$$\overline{U}_0 = \sigma_0 \frac{\partial u_x}{\partial x} + \frac{1}{2}\sigma_0 \begin{Bmatrix} \frac{\partial u_x}{\partial x} \\ \frac{\partial u_y}{\partial x} \\ \frac{\partial u_z}{\partial x} \end{Bmatrix}^T \begin{Bmatrix} \frac{\partial u_x}{\partial x} \\ \frac{\partial u_y}{\partial x} \\ \frac{\partial u_z}{\partial x} \end{Bmatrix} + \frac{1}{2}\left(\frac{\partial u_x}{\partial x}\right)^T E_t \left(\frac{\partial u_x}{\partial x}\right), \tag{15}$$

which becomes, after using Eq. (14),

$$\begin{aligned} \overline{U}_0 = \mathbf{u}_e^T \sigma_0 \begin{bmatrix} -\frac{1}{L} & 0 & 0 & \frac{1}{L} & 0 & 0 \end{bmatrix}^T + \frac{1}{2}\mathbf{u}_e^T \sigma_0 \mathbf{B}^T \mathbf{B} \mathbf{u}_e + \\ \frac{1}{2}\mathbf{u}_e^T \begin{bmatrix} -\frac{1}{L} & 0 & 0 & \frac{1}{L} & 0 & 0 \end{bmatrix}^T E_t \begin{bmatrix} -\frac{1}{L} & 0 & 0 & \frac{1}{L} & 0 & 0 \end{bmatrix} \mathbf{u}_e . \end{aligned} \tag{16}$$

Equation (9) represents the increase in strain energy density in a one-dimensional element subjected to a general three-dimensional displacement field in terms of its nodal displacements. Thus, its associated total strain energy increase is given by

$$U = \int_V \overline{U}_0 \, dV , \tag{17}$$

which becomes, for an element with constant cross section A and length L,

$$U = \int_0^L \int_A \overline{U}_0 \, dA \, dx = \int_0^L A\overline{U}_0 \, dx , \tag{18}$$

which becomes, after substituting Eq. (16),

$$U = -\mathbf{u}_e^T \mathbf{F}_0 + \frac{1}{2}\mathbf{u}_e^T \mathbf{k}_c \mathbf{u}_e + \frac{1}{2}\mathbf{u}_e^T \mathbf{k}_r \mathbf{u}_e , \tag{19}$$

where terms $\mathbf{F}_0$, $\mathbf{k}_c$, and $\mathbf{k}_r$ are given by

$$\begin{aligned} \mathbf{F}_0 &= A\sigma_0 \begin{bmatrix} 1 & 0 & 0 & -1 & 0 & 0 \end{bmatrix}^T , \\ \mathbf{k}_c &= A\sigma_0 \int_0^L \mathbf{B}^T \mathbf{B} \, dx = \frac{A\sigma_0}{L} \begin{bmatrix} \mathbf{I}_3 & -\mathbf{I}_3 \\ -\mathbf{I}_3 & \mathbf{I}_3 \end{bmatrix} , \\ \mathbf{k}_r &= AE_t \int_0^L \begin{bmatrix} -\frac{1}{L} \\ 0 \\ 0 \\ \frac{1}{L} \\ 0 \\ 0 \end{bmatrix} \begin{bmatrix} -\frac{1}{L} \\ 0 \\ 0 \\ \frac{1}{L} \\ 0 \\ 0 \end{bmatrix}^T dx = \frac{AE_t}{L} \begin{bmatrix} 1 & 0 & 0 & -1 & 0 & 0 \\ 0 & 0 & 0 & 0 & 0 & 0 \\ 0 & 0 & 0 & 0 & 0 & 0 \\ -1 & 0 & 0 & 1 & 0 & 0 \\ 0 & 0 & 0 & 0 & 0 & 0 \\ 0 & 0 & 0 & 0 & 0 & 0 \end{bmatrix} . \end{aligned} \tag{20}$$

The first term in Eq. (19) refers to the load vector produced by internal stresses ($\mathbf{F}_0$), and the second and third terms refer, respectively, to stiffness matrices related with stress stiffening ($\mathbf{k}_c$) and longitudinal (rod-like) stiffness ($\mathbf{k}_r$) of the one-dimensional element. These components also indicate that the stiffness is dominant in the longitudinal behavior, while string tension is responsible for transverse behavior, as pointed out in [4].

In the case of dynamic analyses, inertia effects must be accounted. Thus, the instantaneous kinetic energy T can be written for the one-dimensional element with constant mass density ρ using the time derivative notation $\dot{\mathbf{u}} = \frac{\partial \mathbf{u}}{\partial t}$ and Eq. (11) as

$$T = \int_V \frac{1}{2} |\dot{\mathbf{u}}|^2 \, dm = \int_V \frac{1}{2} \dot{\mathbf{u}}^T \dot{\mathbf{u}} \, dm = \int_0^L \int_A \frac{1}{2} \dot{\mathbf{u}}_e^T \mathbf{N}^T \mathbf{N} \dot{\mathbf{u}}_e \, \rho \, dA \, dx ,$$

which leads to

$$T = \frac{1}{2}\dot{\mathbf{u}}_e^T \mathbf{m} \dot{\mathbf{u}}_e \,, \tag{21}$$

where $\mathbf{m}$ is the consistent mass matrix, given by

$$\mathbf{m} = \rho A \int_0^L \mathbf{N}^T \mathbf{N}\, dx = \frac{\rho A L}{6} \begin{bmatrix} 2\mathbf{I}_3 & \mathbf{I}_3 \\ \mathbf{I}_3 & 2\mathbf{I}_3 \end{bmatrix} . \tag{22}$$

3.2 Damping matrices

The introduction of damping is accomplished by considering damping ratios relative to a chosen vibration mode. This can be done by writing the orthonormal matrix $\mathbf{\Psi}$, obtained using a base relative to in-phase and anti-phase modes, described by

$$\mathbf{\Psi} = \frac{1}{\sqrt{2}} \begin{bmatrix} \mathbf{I}_3 & \mathbf{I}_3 \\ \mathbf{I}_3 & -\mathbf{I}_3 \end{bmatrix} . \tag{23}$$

This matrix can be used to obtain diagonal stiffness ($\tilde{\mathbf{k}}$) and mass ($\tilde{\mathbf{m}}$) matrices, which represent vibration in a modal basis, respectively given by

$$\begin{aligned} \tilde{\mathbf{k}} &= \mathbf{\Psi}^T(\mathbf{k}_c + \mathbf{k}_r)\mathbf{\Psi} = \mathrm{diag}\left(0, \quad 0, \quad 0, \quad 2A(E_t + \sigma_0)/L, \quad 2A\sigma_0/L, \quad 2A\sigma_0/L\right) , \\ \tilde{\mathbf{m}} &= \mathbf{\Psi}^T \mathbf{m} \mathbf{\Psi} = \mathrm{diag}\left(\rho AL/2, \quad \rho AL/2, \quad \rho AL/2, \quad \rho AL/6, \quad \rho AL/6, \quad \rho AL/6\right) . \end{aligned} \tag{24}$$

Computing the i-th natural frequency using $\omega_i^2 = \tilde{k}_i/\tilde{m}_i$, where i indicates the i-th component of matrices $\tilde{\mathbf{k}}$ and $\tilde{\mathbf{m}}$, respectively, three zero-frequency (rigid body) modes are obtained, while the remaining three frequency values are related with one longitudinal and two transversal body modes, respectively given by

$$\omega_l = \sqrt{\frac{12(E_t + \sigma_0)}{\rho L^2}} \,, \omega_t = \sqrt{\frac{12\sigma_0}{\rho L^2}} \,. \tag{25}$$

The damping ratio of a single degree-of-freedom system with a particle of mass m, subjected to forces yielded by a spring-dashpot system with stiffness k and damping coefficient c is defined as [5]

$$\xi = \frac{c}{2\sqrt{km}} \,. \tag{26}$$

Assuming structural damping, the diagonal damping matrix can be written as

$$\tilde{\mathbf{c}} = \alpha \tilde{\mathbf{m}} + \beta \tilde{\mathbf{k}} \,, \tag{27}$$

where α and β are proportional factors. By considering the i-th term of diagonal matrices $\tilde{\mathbf{k}}$ and $\tilde{\mathbf{m}}$, one has

$$\xi = \frac{\alpha m_i + \beta k_i}{2\sqrt{k_i m_i}} = \frac{1}{2}\left(\frac{\alpha}{\omega} + \beta\omega\right) , \tag{28}$$

which can be solved to yield given ξ values as ω_l and ω_t, yielding

$$\begin{aligned} \alpha &= \frac{2\xi\omega_l\omega_t}{\omega_l + \omega_t} \,, \\ \beta &= \frac{2\xi}{\omega_l + \omega_t} \,. \end{aligned} \tag{29}$$

Thus, the damping matrix in the original coordinate system can be obtained as

$$\mathbf{c} = \mathbf{\Psi}\tilde{\mathbf{c}}\mathbf{\Psi}^T = \alpha\mathbf{m} + \beta\mathbf{k} = \frac{2\xi\omega_l\omega_t}{\omega_l + \omega_t}\mathbf{m} + \frac{2\xi}{\omega_l + \omega_t}(\mathbf{k}_c + \mathbf{k}_r) \,. \tag{30}$$

The general form of the damping matrix expressed in Eq. (30) allows to consider distinct damping ratio values for radial and spiral threads, which can be obtained from the literature. In our case, we have considered the value of 0.12 damping ratio for spiral threads and 0.075 for radial threads [6].

4 Finite element time series procedures

4.1 Structure stabilization

Prior to time series computations, the structure needs to be checked for stability in terms of residual internal forces which may arise due to imposed initial stresses which possibly are not in equilibrium at a given geometric configuration. In this case, a static procedure is adopted, which corresponds to letting the structure adjust its geometric configuration to achieve force balance for all elements.
To account for nonlinear material characteristics, we adopted a Newton-Raphson static method in the form [2]

$$\begin{aligned} \mathbf{K}_t^{(i-1)} \Delta \mathbf{U}^{(i)} &= \mathbf{F}_{\text{ext}} - \mathbf{F}_{\text{int}}^{(i-1)} \,, \\ \mathbf{U}^{(i)} &= \mathbf{U}^{(i-1)} + \Delta \mathbf{U}^{(i)} \,, \end{aligned} \tag{31}$$

where $\mathbf{K}_t$ corresponds to the tangent stiffness matrix obtained by the usual assembly process [3] of matrices shown in Eq. (20) computed for a given geometric configuration and stress distribution, $\mathbf{F}_{\text{ext}}$ is the load vector of external forces, $\mathbf{F}_{\text{int}}$ is the load vector of forces necessary to produce the current state of stress (opposite sign as $\mathbf{F}_0$ in Eq. (20)), and $\Delta\mathbf{U}$ is the increment in displacement in consecutive iterations. This process is repeated until convergence is reached, i.e., $|\mathbf{F}_{\text{ext}} - \mathbf{F}_{\text{int}}|^{(i-1)} < F_{\text{tol}}$. In the case of initial stabilization procedures, $\mathbf{F}_{\text{ext}} = \mathbf{0}$, $\mathbf{U}^{(0)} = \mathbf{0}$, and $F_{\text{tol}} = 2.22 \times 10^{-16}$ N was adopted.

4.2 Time series computation

For the computation of time responses, two distinct approaches are considered. In the purely linear approach, stiffness and mass matrices $\mathbf{K}$ and $\mathbf{M}$ are assembled [3] at the current geometric configuration and stress state of elements using the element stiffness matrices ($\mathbf{k}_c$ and $\mathbf{k}_r$) given by Eq. (20) and the element mass matrix ($\mathbf{m}$) given by Eq. (22). In this case, the nonlinear stress-strain curves are disregarded throughout the time steps, being considered only for the initial state. Then, an implicit integration scheme such as the Newmark method [2, 7] is applied to obtain displacements at the time instant $t + \Delta t$ in the form

$$\begin{aligned} &\left(\mathbf{K} + \frac{1}{\alpha \Delta t^2} \mathbf{M} + \frac{\delta}{\alpha \Delta t} \mathbf{C} \right) \mathbf{U}(t + \Delta t) = \mathbf{F}_{\text{ext}}(t + \Delta t) \\ &+ \mathbf{M} \left(\frac{1}{\alpha \Delta t^2} \mathbf{U}(t) + \frac{1}{\alpha \Delta t} \dot{\mathbf{U}}(t) + \frac{1 - 2\alpha}{2\alpha} \ddot{\mathbf{U}}(t) \right) + \mathbf{C} \left(\frac{\delta}{\alpha \Delta t} \mathbf{U}(t) + \frac{\delta - \alpha}{\alpha} \dot{\mathbf{U}}(t) + \frac{\Delta t}{2} \frac{\delta - 2\alpha}{\alpha} \ddot{\mathbf{U}}(t) \right) \end{aligned} \tag{32}$$

where Δt is the time step, constants used for approximations of accelerations are given by $\delta = \frac{1}{2}$ and $\alpha = \frac{1}{4}$, $\mathbf{F}_{\text{ext}}(t)$ is the external load vector at time t, and $\mathbf{U}(t)$, $\dot{\mathbf{U}}(t)$, and $\ddot{\mathbf{U}}(t)$ correspond to the nodal displacement, velocity, and acceleration vectors at time t. Velocities and accelerations are updated according to

$$\begin{aligned} \dot{\mathbf{U}}(t + \Delta t) &= \dot{\mathbf{U}}(t) + \Delta t (1 - \delta) \ddot{\mathbf{U}}(t) + \delta \Delta t \ddot{\mathbf{U}}(t + \Delta t) \,, \\ \ddot{\mathbf{U}}(t + \Delta t) &= \frac{1}{\alpha \Delta t^2} \left(\mathbf{U}(t + \Delta t) - \mathbf{U}(t) \right) - \frac{1}{\alpha \Delta t} \dot{\mathbf{U}}(t) - \frac{1 - 2\alpha}{2\alpha} \ddot{\mathbf{U}}(t) \,. \end{aligned} \tag{33}$$

For the nonlinear cases, a explicit time integration is performed in the form

$$\mathbf{M} \ddot{\mathbf{U}}(t) = \mathbf{F}_{\text{ext}}(t) - \mathbf{F}_{\text{int}}(t) \,, \tag{34}$$

where the nodal internal forces vector $\mathbf{F}_{\text{int}}(t)$, which considers the nonlinear stress-strain curves of materials, corresponds to the loads necessary to produce that state of stress at time t. Accelerations are then computed using a central difference approximation as

$$\ddot{\mathbf{U}}(t) = \frac{1}{\Delta t^2} \left(\mathbf{U}(t - \Delta t) - 2\mathbf{U}(t) + \mathbf{U}(t + \Delta t) \right) . \tag{35}$$

Equation (34) and (35) can be combined to yield the time series increment scheme

$$\mathbf{U}(t+\Delta t) = 2\mathbf{U}(t) - \mathbf{U}(t-\Delta t) + \Delta t^2 \mathbf{M}^{-1}(\mathbf{F}_{\text{ext}}(t) - \mathbf{F}_{\text{int}}(t))\,. \tag{36}$$

For the tested cases, using sufficiently small time steps, this iteration scheme has yielded the same results as other (iterative) implicit integration methods, such as the nonlinear Newmark method (see references [2, 8, 9] for details).

5 Dispersion relation

To compute the dispersion relation (i.e., relation between wavenumbers and frequencies), let us initially consider a two-node (nodes i and j) finite element whose stiffness and mass matrices $\mathbf{K}$ and $\mathbf{M}$, previously presented in 3, relate to displacements $\mathbf{u}$ and external applied forces $\mathbf{f}$ as

$$\mathbf{M}\ddot{\mathbf{u}} + \mathbf{K}\mathbf{u} = \mathbf{f}\,, \tag{37}$$

which, assuming time-harmonic displacements $\mathbf{u} = \hat{\mathbf{u}}e^{\mathrm{i}\omega t}$ and forces $\mathbf{f} = \hat{\mathbf{f}}e^{\mathrm{i}\omega t}$ lead to

$$(\mathbf{K} - \omega^2\mathbf{M})\hat{\mathbf{u}} = \hat{\mathbf{f}}\,. \tag{38}$$

Partitioning displacements and forces using indexes relative to nodes i and j, respectively, yields

$$\left(\begin{bmatrix} \mathbf{K}_{ij} & \mathbf{K}_{ij} \\ \mathbf{K}_{ji} & \mathbf{K}_{jj} \end{bmatrix} - \omega^2 \begin{bmatrix} \mathbf{M}_{ii} & \mathbf{M}_{ij} \\ \mathbf{M}_{ji} & \mathbf{M}_{jj} \end{bmatrix} \right) \begin{Bmatrix} \hat{\mathbf{u}}_i \\ \hat{\mathbf{u}}_j \end{Bmatrix} = \begin{Bmatrix} \hat{\mathbf{f}}_i \\ \hat{\mathbf{f}}_j \end{Bmatrix}\,. \tag{39}$$

Considering such an element of length L subjected to periodic boundary conditions, Bloch-Floquet conditions [10] may apply, yielding

$$\hat{\mathbf{u}}_j = \lambda \hat{\mathbf{u}}_i\,, \tag{40a}$$

$$\hat{\mathbf{f}}_i + \lambda^{-1}\hat{\mathbf{f}}_j \tag{40b}$$

where $\lambda = e^{\mathrm{i}kL}$, with $\mathrm{i} = \sqrt{-1}$, and k is the complex wavenumber.
Combining Eqs. (39) and (40) yields

$$\begin{bmatrix} \mathbf{I} & \lambda^{-1}\mathbf{I} \end{bmatrix} \left(\begin{bmatrix} \mathbf{K}_{ii} & \mathbf{K}_{ij} \\ \mathbf{K}_{ji} & \mathbf{K}_{jj} \end{bmatrix} - \omega^2 \begin{bmatrix} \mathbf{M}_{ii} & \mathbf{M}_{ij} \\ \mathbf{M}_{ji} & \mathbf{M}_{jj} \end{bmatrix} \right) \begin{bmatrix} \mathbf{I} \\ \lambda\mathbf{I} \end{bmatrix} \hat{\mathbf{u}}_i = \begin{bmatrix} \mathbf{I} & \lambda^{-1}\mathbf{I} \end{bmatrix} \begin{Bmatrix} \hat{\mathbf{f}}_i \\ \hat{\mathbf{f}}_j \end{Bmatrix} = \mathbf{0}\,, \tag{41}$$

which leads to the eigenvalue problem stated as

$$\Big((\mathbf{K}_{ii} + \lambda^{-1}\mathbf{K}_{ji} + \lambda\mathbf{K}_{ij} + \mathbf{K}_{jj}) - \omega^2(\mathbf{M}_{ii} + \lambda^{-1}\mathbf{M}_{ji} + \lambda\mathbf{M}_{ij} + \mathbf{M}_{jj}) \Big)\hat{\mathbf{u}}_i = \mathbf{0}\,, \tag{42}$$

which admits nontrivial solutions for

$$\det\left((\mathbf{K}_{ii} + \lambda^{-1}\mathbf{K}_{ji} + \lambda\mathbf{K}_{ij} + \mathbf{K}_{jj}) - \omega^2(\mathbf{M}_{ii} + \lambda^{-1}\mathbf{M}_{ji} + \lambda\mathbf{M}_{ij} + \mathbf{M}_{jj}) \right) = 0\,. \tag{43}$$

Recalling matrix definitions from Eqs. (20) and (22), matrix partitioning yields

$$\mathbf{K}_{ii} = \mathbf{K}_{jj} = \begin{bmatrix} A(E_t + \sigma_0)/L & 0 & 0 \\ 0 & A\sigma_0/L & 0 \\ 0 & 0 & A\sigma_0/L \end{bmatrix},\ \mathbf{K}_{ij} = \mathbf{K}_{ji} = -\mathbf{K}_{ii}\,, \tag{44a}$$

$$\mathbf{M}_{ii} = \mathbf{M}_{jj} = \frac{\rho AL}{3}\mathbf{I},\ \mathbf{M}_{ij} = \mathbf{M}_{ji} = \frac{\rho AL}{6}\mathbf{I}\,, \tag{44b}$$

$$\tag{44c}$$

.

Solving Eq. (43) for λ under the assumptions $\sigma_0 \gg \rho L^2\omega^2$ and $E_t \gg \rho L^2\omega^2$, valid for low frequencies, yields the approximated solutions

$$\lambda_{1,2} = -1 \pm \mathrm{i}\sqrt{\frac{\rho}{\sigma_0}}L\omega\,, \tag{45a}$$

$$\lambda_{3,4} = 1 \pm \mathrm{i}\sqrt{\frac{\rho}{E_t+\sigma_0}}L\omega\,, \tag{45b}$$

which yields the approximated dispersion relations

$$k_{1,2} = \sqrt{\frac{\rho}{\sigma_0}}\omega\,, k_{3,4} = \sqrt{\frac{\rho}{E_t+\sigma_0}}\omega\,, \tag{46}$$

which indicate a non-dispersive relation [11], thus indicating waves are purely propagating, not presenting an evanescent behavior [12]. Also, the transverse (c_t) and longitudinal (c_l) wave speeds are given by

$$c_t = \frac{\omega}{k_{1,2}} = \sqrt{\frac{\sigma_0}{\rho}}\,, c_l = \frac{\omega}{k_{3,4}} = \sqrt{\frac{E_t+\sigma_0}{\rho}}\,. \tag{47}$$

6 Glue degradation

To evaluate the effect of the degradation of the connecting elements between radial and spiral threads, we have also performed vibration analyses concerning the baseline impact point (Section 3.3.1) and degraded mechanical behavior for the connection elements. Since we initially considered glue as having the same properties as spiral threads, we now model glue degradation using a softening behavior, considering it having only 25% of the stress-strain relation of viscid threads. Results are shown in **Figure** 3.

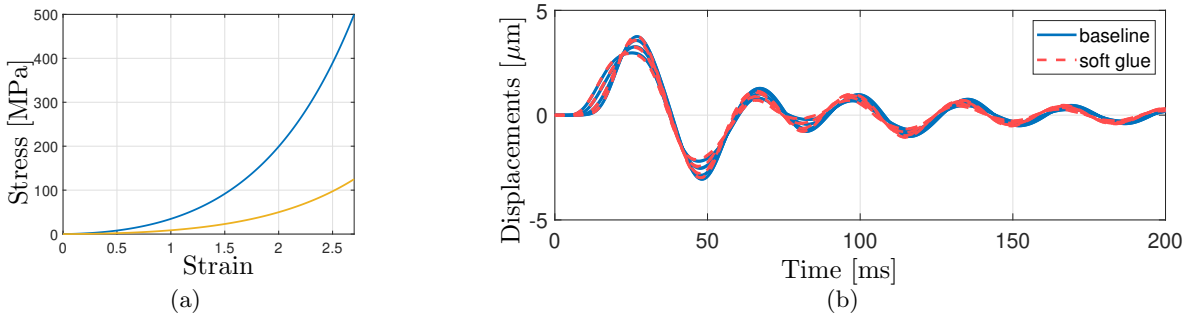

Figure 3: Results for assessing the effects of glue degradation. (a) The degradation in (■) glue is modeled as a proportional factor of the stress-strain behavior of (■) spiral threads. (b) The results of considering this soft glue are not noticeable in the output displacements.

Figure 3a show the stress-strain curves for the gluing elements, considered as a softer version of the spiral threads to model its degradation. Figure 3b shows the variation of output displacements. Changes in such computed displacements are barely noticeable, thus indicating that this orb web architecture is likely robust against variations in the connections between radial and spiral threads.

References

[1] S. W. Cranford, A. Tarakanova, N. M. Pugno, M. J. Buehler, *Nature* **2012**, *482*, 7383 72.

[2] K. J. Bathe, *Finite Element Procedures*, Prentice-Hall International Series in. Prentice Hall, **1996**.

[3] R. D. Cook, D. S. Malkus, M. E. Plesha, R. J. Witt, *Concepts and Applications of Finite Element Analysis*, Wiley, 4 edition, **2001**.

[4] I. G. Main, *Vibrations and Waves in Physics*, Cambridge University Press, **1993**.

[5] D. J. Inman, R. C. Singh, *Engineering vibration*, volume 3, Prentice Hall Englewood Cliffs, NJ, **1994**.

[6] R. Das, A. Kumar, A. Patel, S. Vijay, S. Saurabh, N. Kumar, *Journal of the Mechanical Behavior of Biomedical Materials* **2017**, *67* 101.

[7] N. M. Newmark, *Journal of the Engineering Mechanics Division* **1959**, *85*, 3 67.

[8] M. A. Dokainish, K. Subbaraj, *Computers & Structures* **1989**, *32*, 6 1371.

[9] K. Subbaraj, M. A. Dokainish, *Computers & Structures* **1989**, *32*, 6 1387.

[10] F. Bloch, *Zeitschrift für Physik* **1929**, *52*, 7-8 555.

[11] U. Lee, *Spectral Element Method in Structural Dynamics*, John Wiley & Sons, **2009**.

[12] V. Laude, Y. Achaoui, S. Benchabane, A. Khelif, *Physical Review B* **2009**, *80*, 9 092301.